ISSN 1560-3547, Regular and Chaotic Dynamics, 2020, Vol. 25, No. 6, pp. 553–580. © Pleiades Publishing, Ltd., 2020.

The Tippedisk: a Tippetop Without Rotational Symmetry

Simon Sailer[1*], Simon R. Eugster[1], and Remco I. Leine[1***]**

[1] *Institute for Nonlinear Mechanics, University of Stuttgart, Pfaffenwaldring 9, 70569 Stuttgart, Germany*

Received July 24, 2020; revised September 28, 2020; accepted October 16, 2020

Abstract—The aim of this paper is to introduce the *tippedisk* to the theoretical mechanics community as a new mechanical-mathematical archetype for friction induced instability phenomena. We discuss the modeling and simulation of the tippedisk, which is an inhomogeneous disk showing an inversion phenomenon similar but more complicated than the tippetop. In particular, several models with different levels of abstraction, parameterizations and force laws are introduced. Moreover, the numerical simulations are compared qualitatively with recordings from a high-speed camera. Unlike the tippetop, the tippedisk has no rotational symmetry, which greatly complicates the three-dimensional nonlinear kinematics. The governing differential equations, which are presented here in full detail, describe all relevant physical effects and serve as a starting point for further research.

MSC2010 numbers: 70E18, 70K20, 70E50

DOI: 10.1134/S1560354720060052

Keywords: gyroscopic system, friction, contact modelling, dynamics, inversion phenomenon

1. INTRODUCTION

Various gyroscopic systems which are interacting with a horizontal frictional support, such as rolling and sliding disks [3, 5, 15, 25, 27], Euler's disk [14, 16, 20], the rattleback [4, 8] and the tippetop [6, 7, 13, 19, 28], form a scientific playground for research in theoretical mechanics. The tippetop belongs to a subclass of gyroscopic systems which shows inversion phenomena. The tippetop is a rotationally symmetric top, consisting of a spherical body and a stem attached to it, see Fig. 1. The center of gravity (COG) does not coincide with the geometric center, such that the stem points upwards as the top rotates slowly with noninverted orientation. When the top is spun fast around its axis of symmetry, the gravitational, normal, and friction forces acting on the top cause the top to invert its orientation, such that it finally balances on its stem. This phenomenon of inversion also occurs for other axisymmetric bodies with rotational symmetry in inertia and geometry, for example, hard-boiled spinning eggs [21, 22] or the science toy called "PhiTOP"[1)], which is basically the symmetric equivalent of a hard-boiled spinning egg. But what happens if rotational symmetry does not exist? This is the topic of the present paper.

The "orbit spinning top" is a commercial toy consisting of a thin disk and an eccentrically attached sphere. If this top is spun around an in-plane axis, the center of gravity rises until the top is spinning in an inverted configuration[2)]. Similar to the orbit spinning top, an eccentric disk also shows this kind of inversion and faced a huge interest on social media[3),4)]. In Fig. 2 the inversion process of the tippedisk is depicted in a stroboscopic photo sequence, which comes from

*E-mail: sailer@inm.uni-stuttgart.de

**E-mail: eugster@inm.uni-stuttgart.de

***E-mail: leine@inm.uni-stuttgart.de

[1)] http://www.thephitop.com/

[2)] Youtube: Orbit Spinning Tops (https://www.youtube.com/watch?v=9pV7iaaR1QY)

[3)] Youtube: Spinning Disk Trick (https://www.youtube.com/watch?v=h0SZZTBQmEs)

[4)] Youtube: Spinning Disk Trick Solution (https://www.youtube.com/watch?v=tDr26U49_VA)

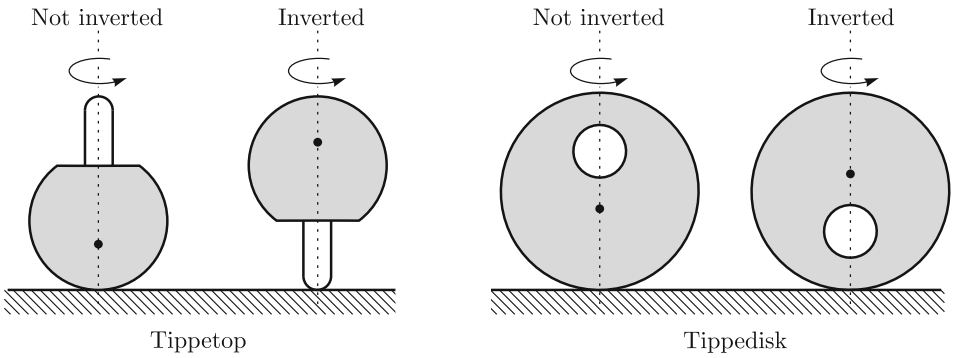

Fig. 1. Inversion phenomenon showing the rise of the COG (black dot).

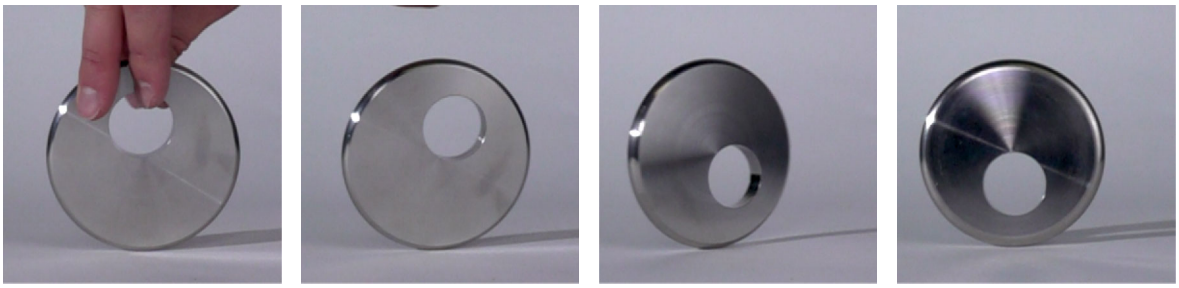

Fig. 2. Tippedisk: inversion phenomenon.

an experiment. The only sources which mention or discuss the inversion phenomenon of asymmetric disks are nonacademic and either from social media or from websites of producers of scientific toys.

According to many hobby scientists on such platforms, the Dzhannibekov effect is responsible for this phenomenon. This Dzhannibekov effect is also known as the tennis racket theorem[5)] or the intermediate axis theorem and describes the recurring flipping between two unstable stationary solutions for a free spinning rigid body [2, 26]. In contrast, the inversion process only occurs once for an eccentric spinning disk on a frictional support, which is why the Dzhannibekov effect cannot be attributed to this phenomenon. All existing explanations are based on intuitive considerations and pseudo-scientific statements such as "the disk inverts because this is energetically beneficial" which lack scientific rigor. The symmetric spinning disk is well understood in the sense of Euler's disk [14, 20] or in the sense of spinning or rolling coins [15, 25]. The unbalanced disk treated in the context of rotor dynamics [30] has nothing to do with the asymmetric disk with contact. The only academic work which deals with the unbalanced disk on a frictional support is [12]. This work only mentions the inversion phenomenon, but does not deal with it, so there is no scientific discussion. As this system has not been studied by the scientific community and is currently lacking an identifiable scientific name, we propose calling it the "tippedisk" in analogy to the tippetop. In this work we introduce the "tippedisk" as a new archetype of a three-dimensional rigid body system with frictional contact. The tippedisk can be seen as a thin disk for which the COG does not coincide with its geometric center, see Fig. 1. If the tippedisk is spun around an in-plane axis, one can observe that the COG rises until the disk remains in an inverted configuration. The inversion phenomenon is therefore not restricted to axisymmetric rigid bodies and also takes place for rigid bodies like the tippedisk.

The aim of this paper is to develop a mathematical model which can form the basis for a closed form analysis as well as for numerical simulations of the inversion phenomenon. As the disk is allowed to detach and its qualitative behavior is strongly influenced by the acting dissipation mechanisms, we use set-valued force laws as a starting point. The description within Nonsmooth Dynamics using set-valued force laws is necessary, since single-valued force laws are only approximately capable of describing unilateral frictional contact. We will derive a quaternion-based

[5)] https://rotations.berkeley.edu/a-tumbling-t-handle-in-space/

model and a model in Euler angles. Each of these parameterizations has its own advantages. The quaternion-based parameterization is well suited for numerical simulations. The model in Euler angles leads to numerical difficulties, as the parameterization can become singular but is more suitable for closed form analysis of the nonlinear behavior. Numerical simulations in Euler angles are always accompanied by numerical simulation with quaternions to check the accuracy of the simulation in Euler angles. In Section 2, we introduce the kinematics, kinetics, and force laws of the model and set notation. Section 3 describes the parameterizations which are used to obtain the equations of motion. Numerical techniques to solve the system equations obtained, using dimensions from Section 5, are discussed in Section 4. In Section 6 numerical results are presented, which are subsequently discussed in Section 7.

2. MECHANICAL MODEL OF THE TIPPEDISK

The mechanical system as depicted in Fig. 3 consists of a rigid disk with mass m, radius r, eccentricity e and a flat frictional support. Since we are only interested in the main physical phenomena, we approximate the disk as an infinitely thin disk and therefore neglect its thickness and assume the contact point to lie on a circle around the geometric center G. The disk and support are considered to be rigid.

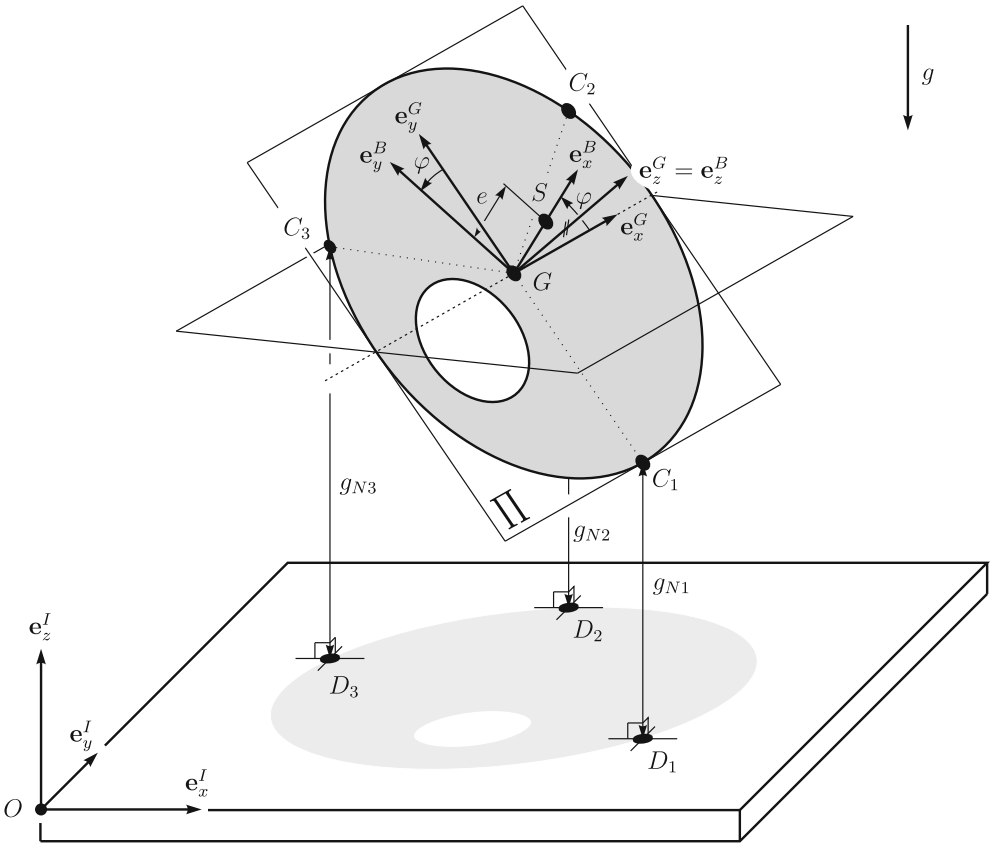

Fig. 3. Mechanical model: tippedisk.

We introduce an orthonormal inertial frame $I = (O, \mathbf{e}_x^I, \mathbf{e}_y^I, \mathbf{e}_z^I)$ attached to the origin O, where $\mathbf{e}_z^I$ is normal to the flat support. The right-handed body-fixed frame $B = (G, \mathbf{e}_x^B, \mathbf{e}_y^B, \mathbf{e}_z^B)$ is attached to the geometric center G of the disk, such that $\mathbf{e}_z^B$ is normal to the surface of the disk. The axis $\mathbf{e}_x^B$ is defined as the normalized vector of $\mathbf{r}_{GS}$, which points from the geometric center G to the center of gravity S. The inertia tensor with respect to G expressed in the body-fixed B-frame is given as ${}_B\mathbf{\Theta}_G = \operatorname{diag}(A, B, C)$, where $B < A < C$ holds. For the interaction between disk and support, the

point with minimal height is introduced as C_1. Following [15], we define two additional points C_2 and C_3 to describe also motions for which one face of the disk is in contact with the flat support.

The Cartesian coordinate representation of a vector $\mathbf{a} \in \mathbb{E}^3$ in an arbitrary orthonormal D-frame rotated against the I-frame is denoted as ${}_D\mathbf{a} = (a_x^D,\, a_y^D,\, a_z^D)^{\mathrm{T}} \in \mathbb{R}^3$ with $\mathbf{a} = a_x^D \mathbf{e}_x^D + a_y^D \mathbf{e}_y^D + a_z^D \mathbf{e}_z^D \in \mathbb{E}^3$. The orthogonal transformation matrix $\mathbf{A}_{ID} \in \mathbb{R}^{3\times 3}$ relates the respective coordinates in accordance with ${}_I\mathbf{a} = \mathbf{A}_{ID}\, {}_D\mathbf{a}$ and corresponds with the coordinates of the D-frame basis vectors in the I-frame, i. e., $\mathbf{A}_{ID} = [{}_I\mathbf{e}_x^D,\, {}_I\mathbf{e}_y^D,\, {}_I\mathbf{e}_z^D] \in \mathbb{R}^{3\times 3}$. The inverse of the transformation matrix $\mathbf{A}_{ID}$ is denoted as $\mathbf{A}_{DI} = \mathbf{A}_{ID}^{-1} = \mathbf{A}_{DI}^{\mathrm{T}}$. The rotation matrix $\mathbf{R} \in \mathcal{SO}(3)$ links the body-fixed B-frame with the inertial I-frame by ${}_I\mathbf{e}_i^B = \mathbf{R}\, {}_I\mathbf{e}_i^I$ for $i \in \{x, y, z\}$ and can thus be expressed as

$$\mathbf{R} = \left[\, {}_I\mathbf{e}_x^B \quad {}_I\mathbf{e}_y^B \quad {}_I\mathbf{e}_z^B \,\right] = \mathbf{A}_{IB}, \tag{2.1}$$

with the properties $\mathbf{R}\mathbf{R}^{\mathrm{T}} = \mathbf{R}^{\mathrm{T}}\mathbf{R} = \mathbf{I}$ and $\det(\mathbf{R}) = +1$. Using the bijective map

$$j: \quad \mathbb{R}^3 \to \mathbb{R}^{3\times 3}: \quad \mathbf{a} = \begin{bmatrix} a_1 \\ a_2 \\ a_3 \end{bmatrix} \mapsto \tilde{\mathbf{a}} = \begin{bmatrix} 0 & -a_3 & a_2 \\ a_3 & 0 & -a_1 \\ -a_2 & a_1 & 0 \end{bmatrix}, \tag{2.2}$$

we define the angular velocity ${}_B\boldsymbol{\Omega} = [\omega_x,\, \omega_y,\, \omega_z]^{\mathrm{T}}$ of the tippedisk, expressed in the body-fixed B-frame, as

$${}_B\boldsymbol{\Omega} := j^{-1}(\mathbf{R}^{\mathrm{T}}\dot{\mathbf{R}}). \tag{2.3}$$

The differentiation with respect to time t is indicated by the dot $(\dot{\ }) = \frac{\mathrm{d}}{\mathrm{d}t}(\ )$. By ${}_B\dot{\mathbf{a}} = ({}_B\mathbf{a})\dot{}$, we denote the time derivative of the components of the vector $\mathbf{a}$ expressed in the moving B-frame. The absolute time derivative $\dot{\mathbf{a}}$ of the vector $\mathbf{a}$, expressed in the B-frame, follows as

$${}_B(\dot{\mathbf{a}}) = {}_B\dot{\mathbf{a}} + {}_B\boldsymbol{\Omega} \times {}_B\mathbf{a}. \tag{2.4}$$

Applying (2.4) on the angular velocity ${}_B\boldsymbol{\Omega}$ from (2.3), and noting ${}_B\boldsymbol{\Omega} \times {}_B\boldsymbol{\Omega} = 0$, results in the angular acceleration $\boldsymbol{\Psi}$

$${}_B\boldsymbol{\Psi} = {}_B\dot{\boldsymbol{\Omega}}. \tag{2.5}$$

The position vector of the geometric center G relative to the origin O is denoted as $\mathbf{r}_{OG}$ and we denote the velocity and acceleration of the point G as $\mathbf{v}_G = \dot{\mathbf{r}}_{OG}$ and $\mathbf{a}_G = \dot{\mathbf{v}}_G = \ddot{\mathbf{r}}_{OG}$. For a rigid body, we can calculate the velocity $\mathbf{v}_P$ of an arbitrary body-fixed point P

$${}_B\mathbf{v}_P = {}_B\mathbf{v}_G + {}_B(\dot{\mathbf{r}}_{GP}) = {}_B\mathbf{v}_G + {}_B\boldsymbol{\Omega} \times {}_B\mathbf{r}_{GP}, \tag{2.6}$$

which is known as rigid body formula and which reads in vectorial form as

$$\mathbf{v}_P = \mathbf{v}_G + \boldsymbol{\Omega} \times \mathbf{r}_{GP}. \tag{2.7}$$

2.1. Contact Kinematics

To describe the kinematics of the points C_i, we introduce a floating frame $G = (G, \mathbf{e}_x^G, \mathbf{e}_y^G, \mathbf{e}_z^G)$, which is attached to the geometric center G. Its unit vector $\mathbf{e}_z^G$ corresponds to $\mathbf{e}_z^B$, such that $\mathbf{e}_z^G \cdot \mathbf{e}_z^B \equiv 1$ holds. Since the cross product $\mathbf{e}_z^I \times \mathbf{e}_z^B$ is perpendicular to $\mathbf{e}_z^I$ and $\mathbf{e}_z^B$, we can define the horizontal unit vector of the floating frame

$$\mathbf{e}_x^G := \frac{\mathbf{e}_z^I \times \mathbf{e}_z^B}{\|\mathbf{e}_z^I \times \mathbf{e}_z^B\|}, \tag{2.8}$$

where the norm

$$\|\mathbf{e}_z^I \times \mathbf{e}_z^B\| = \left[(R_{13})^2 + (R_{23})^2\right]^{1/2} = \left[1 - (R_{33})^2\right]^{1/2} \tag{2.9}$$

is expressed in terms of the components of the rotation matrix $\mathbf{R}$. Definition (2.8) is only valid for nonhorizontal configurations of the disk with $R_{33} \neq 1$. For horizontal configurations, $\mathbf{e}_x^G$ cannot be

determined uniquely and the floating frame G can be chosen arbitrarily, as long as $\mathbf{e}_z^G = \mathbf{e}_z^B$ holds. For numerical evaluation, we use the continuity condition $\mathbf{e}_z^G(t_i) = \mathbf{e}_z^G(t_{i-1})$, i. e., in the case of horizontal configuration we take the G-frame from the previous time step, cf. [15]. If $R_{33} \neq 1$, we can obtain with $\mathbf{e}_y^G := \mathbf{e}_z^B \times \mathbf{e}_x^G$ a right-handed orthonormal frame, such that the floating coordinate frame $G = (G, \mathbf{e}_x^G, \mathbf{e}_y^G, \mathbf{e}_z^G)$ is fully defined. The point C_1 with minimal height can be described with respect to point G as

$$\mathbf{r}_{GC_1} = -r\,\mathbf{e}_y^G. \tag{2.10}$$

If we rotate $\mathbf{r}_{GC_1}$ around $\mathbf{e}_z^G$ with $\pm\frac{2\pi}{3}$, we obtain

$$\mathbf{r}_{GC_2} = -\frac{1}{2}\mathbf{r}_{GC_1} + \frac{\sqrt{3}}{2}\left(\mathbf{e}_z^G \times \mathbf{r}_{GC_1}\right), \quad \mathbf{r}_{GC_3} = -\frac{1}{2}\mathbf{r}_{GC_1} - \frac{\sqrt{3}}{2}\left(\mathbf{e}_z^G \times \mathbf{r}_{GC_1}\right). \tag{2.11}$$

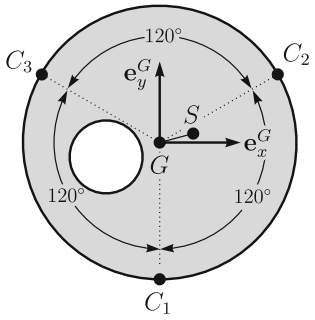

Fig. 4. Contact points C_i.

With (2.10) and (2.11), the three candidate contact points C_1, C_2 and C_3 are defined for nonhorizontal configurations. The gap g_i between each contact point C_i and the flat support is equal to the projection of $\mathbf{r}_{OC_i}$ onto the $\mathbf{e}_z^I$-axis. If we assume a given $\mathbf{r}_{OG}$, the gap functions g_{N_i} are defined with (2.10) and (2.11) as

$$g_{N_i} = \mathbf{r}_{OC_i} \cdot \mathbf{e}_z^I = (\mathbf{r}_{OG} + \mathbf{r}_{GC_i}) \cdot \mathbf{e}_z^I, \quad i = 1, 2, 3. \tag{2.12}$$

The absolute velocity

$$\mathbf{v}_{C_i} = \mathbf{v}_G + \boldsymbol{\Omega} \times \mathbf{r}_{GC_i}, \quad i = 1, 2, 3, \tag{2.13}$$

can be projected onto the orthonormal I-frame leading to the normal relative velocity

$$\gamma_{N_i} := \mathbf{v}_{C_i} \cdot \mathbf{e}_z^I \tag{2.14}$$

and the two-dimensional tangential relative velocity as the 2-tuple

$$\boldsymbol{\gamma}_{T_i} := \begin{bmatrix} \gamma_{Tx_i} \\ \gamma_{Ty_i} \end{bmatrix} = \begin{bmatrix} \mathbf{v}_{C_i} \cdot \mathbf{e}_x^I \\ \mathbf{v}_{C_i} \cdot \mathbf{e}_y^I \end{bmatrix}, \tag{2.15}$$

where γ_{Tx_i} and γ_{Ty_i} are the relative sliding velocities in $\mathbf{e}_x^I$ and $\mathbf{e}_y^I$-direction, respectively. Furthermore, we introduce the pivoting velocity γ_{τ_i} as the relative spin $\omega_{IB} := \boldsymbol{\Omega} \cdot \mathbf{e}_z^I$ scaled with a constant contact radius $\varepsilon_i > 0$

$$\gamma_{\tau_i} := \varepsilon_i\,\omega_{IB}. \tag{2.16}$$

Here, the contact radius ε_i is the radius of the contact area between the disk and the support, which is assumed to be circular, but idealized to be a point (see [17] for further details). With the floating G-frame, we can describe the velocity of the moving contact point C_i, relative to the body-fixed point which momentarily agrees with it, as

$$\gamma_{R_i} := -r\dot{\varphi}. \tag{2.17}$$

2.2. Contact Laws

The contact laws of the contact forces $\mathbf{F}_i \in \mathbb{E}^3$ at the contact points C_i will be described within the framework of Nonsmooth Dynamics [16, 17, 23]. Frictional contact laws have set-valued nature and can conveniently be expressed using normal cone inclusions. To write the force laws as normal cone inclusions, we use the normal cone to a closed convex set $\mathcal{C} \subset \mathbb{R}^n$ at the point $\mathbf{x}$ given by

$$\mathcal{N}_{\mathcal{C}}(\mathbf{x}) := \left\{ \mathbf{y} \in \mathbb{R}^n \;\middle|\; \mathbf{y}^{\mathrm{T}}(\mathbf{x}^* - \mathbf{x}) \leqslant 0, \quad \mathbf{x} \in \mathcal{C}, \forall \mathbf{x}^* \in \mathcal{C} \right\} \tag{2.18}$$

and $\mathcal{N}_{\mathcal{C}}(\mathbf{x}) = \emptyset$ if $\mathbf{x} \notin \mathcal{C}$ holds [29].

2.2.1. Normal direction

In normal direction, we assume a unilateral constraint to prevent the disk from penetration with the support and impose for the normal force λ_{N_i} Signorini's law

$$0 \leqslant g_{N_i} \perp \lambda_{N_i} \geqslant 0, \tag{2.19}$$

which can be formulated on velocity level as

$$g_{N_i} = 0 : \quad 0 \leqslant \gamma_{N_i} \perp \lambda_{N_i} \geqslant 0. \tag{2.20}$$

Following [9, 18, 23], we formulate the generalized Newton's impact law as a normal cone inclusion

$$\xi_{N_i} \in \mathcal{N}_{\mathbb{R}_0^-}(-\Lambda_{N_i}) \quad \text{with} \quad \xi_{N_i} = \gamma_{N_i}^+ + e_{N_i}\gamma_{N_i}^-. \tag{2.21}$$

Here, the parameter e_{N_i} is called the restitution coefficient, $\gamma_{N_i}^+$ and $\gamma_{N_i}^-$ are post- and pre-impact velocities, and Λ_{N_i} denotes the corresponding impulsive force in normal direction [10].

2.2.2. Friction forces

Classical spatial Coulomb friction for the tangential friction forces $\boldsymbol{\lambda}_{T_i}$ is described by the set-valued force law

$$\boldsymbol{\gamma}_{T_i} \in \mathcal{N}_{C_{T_i}}(-\boldsymbol{\lambda}_{T_i}), \tag{2.22}$$

where C_{T_i} is a closed convex set denoting the negative force reservoir. For isotropic friction the negative force reservoir C_{T_i} is equal to a disk with radius $\mu\,\lambda_{N_i}$, where μ is identified as friction coefficient, i.e., $C_{T_i} = \left\{ -\boldsymbol{\lambda}_{T_i} \in \mathbb{R}^2 \middle| \, \|\boldsymbol{\lambda}_{T_i}\| \leqslant \mu\lambda_{N_i} \right\}$. In [17], it was shown that the coupling between sliding friction and pivoting friction is essential for the inversion of the tippetop. The Coulomb – Contensou friction model [17] expresses the coupling between the tangential friction forces $\boldsymbol{\lambda}_T$ and the pivoting torque λ_τ, both of which depend on the tangential sliding velocity $\boldsymbol{\gamma}_{T_i}$ and the scaled angular spin velocity γ_{τ_i}. Together with the triples

$$\boldsymbol{\gamma}_{F_i} = \begin{bmatrix} \boldsymbol{\gamma}_{T_i} \\ \gamma_{\tau_i} \end{bmatrix} \quad \text{and} \quad \boldsymbol{\lambda}_{F_i} = \begin{bmatrix} \boldsymbol{\lambda}_{T_i} \\ \lambda_{\tau_i} \end{bmatrix}, \tag{2.23}$$

the Coulomb – Contensou friction law is formulated as

$$\boldsymbol{\gamma}_{F_i} \in \mathcal{N}_{B_{F_i}}(-\boldsymbol{\lambda}_{F_i}). \tag{2.24}$$

For a parabolic pressure distribution at the contact area with radius ε_i (see [17]), the friction ball $B_{F_i}(\lambda_N)$ can be expressed using

$$\bar{\xi} = \frac{\|\boldsymbol{\lambda}_{T_i}\|}{\mu\lambda_N} \quad \text{and} \quad \bar{\eta} = \frac{\lambda_{\tau_i}}{\mu\lambda_N} \tag{2.25}$$

and

$$\xi^* = \frac{9}{32}\pi \quad \text{and} \quad \eta^* = \frac{9}{128}\pi \tag{2.26}$$

as

$$B_{F_i} := \begin{cases} \left\{ \boldsymbol{\lambda}_{F_i} \middle| \frac{9}{64}\left(\frac{\bar{\eta}}{\eta^*}\right)^2 + \frac{9}{8}\left(\frac{\bar{\xi}}{\xi^*}\right)^2 - \frac{243}{1024}\left(\frac{\bar{\xi}}{\xi^*}\right)^4 + O\left(\left(\frac{\bar{\xi}}{\xi^*}\right)^6\right) \leqslant 1 \right\}, & \bar{\xi} \leqslant \xi^* \\ \left\{ \boldsymbol{\lambda}_{F_i} \middle| \bar{\xi}^2 + 5\bar{\eta}^2 - \frac{75}{7}\bar{\eta}^4 + O(\bar{\eta}^6) \leqslant 1 \right\}, & \bar{\xi} > \xi^*. \end{cases} \tag{2.27}$$

To describe impacts, we restrict us to the classical spatial Coulomb friction impact law [9]

$$\boldsymbol{\xi}_{T_i} \in \mathcal{N}_{C_{T_i}}(-\boldsymbol{\Lambda}_{T_i}) \quad \text{with} \quad \boldsymbol{\xi}_{T_i} = \boldsymbol{\gamma}_{T_i}^+ + e_{T_i}\boldsymbol{\gamma}_{T_i}^-, \tag{2.28}$$

with negative force reservoir C_{T_i}.

The Coulomb – Contensou friction law incorporates the coupling between sliding and pivoting friction and describes the Contensou effect [17]. The set-valued Coulomb friction law for resistance is regularized depending on the pivoting speed γ_τ. For vanishing pivoting speed one retrieves the set-valued Coulomb friction law for sliding, whereas it is strongly regularized for large values of γ_τ. For a fast spinning disk we will have $|\gamma_\tau| \gg \|\boldsymbol{\gamma}_T\|$ which motivates the regularized Coulomb friction law

$$\boldsymbol{\lambda}_{T_i} = -\mu\lambda_{N_i}\frac{\boldsymbol{\gamma}_{T_i}}{\|\boldsymbol{\gamma}_{T_i}\| + \varepsilon}, \tag{2.29}$$

with friction parameter μ and smoothing coefficient ε. As isolated force law for pivoting friction, we assume dry pivoting friction with

$$\gamma_{\tau_i} \in \mathcal{N}_{C_{\tau_i}}(-\lambda_{\tau_i}) \tag{2.30}$$

and the negative force reservoir $C_{\tau_i} := \{x \in \mathbb{R} \,|\, |x| \leqslant \mu_\tau\, \lambda_{N_i}\}$ from [15].

To describe the resistance against rolling, we assume dry contour friction [15]

$$\gamma_{R_i} \in \mathcal{N}_{C_{R_i}}(-\lambda_{R_i}), \tag{2.31}$$

in which C_{R_i} corresponds to the negative force reservoir $C_{R_i} := \{x \in \mathbb{R} \,|\, |x| \leqslant \mu_R\, \lambda_N\}$.

2.3. Virtual Work for a Single Rigid Body

For a single rigid body subjected to the external force $\mathbf{F}_G^{\text{ext}}$ and torque $\mathbf{M}_G^{\text{ext}}$ with respect to the reference point G, with $\mathbf{r}_{GS} = e\,\mathbf{e}_x^B$, the virtual work [9] takes the form

$$\delta W = \begin{bmatrix} \delta\mathbf{r}_G \\ \delta\boldsymbol{\varphi} \end{bmatrix} \cdot \left(\begin{bmatrix} m\,\mathbb{1} & m\tilde{\mathbf{r}}_{GS}^{\mathrm{T}} \\ m\,\tilde{\mathbf{r}}_{GS} & \boldsymbol{\Theta}_G \end{bmatrix} \begin{bmatrix} \mathbf{a}_G \\ \boldsymbol{\Psi} \end{bmatrix} - \begin{bmatrix} -m\,\boldsymbol{\Omega} \times (\boldsymbol{\Omega} \times \mathbf{r}_{GS}) \\ -\boldsymbol{\Omega} \times (\boldsymbol{\Theta}_G\,\boldsymbol{\Omega}) \end{bmatrix} - \begin{bmatrix} \mathbf{F}_G^{\text{ext}} \\ \mathbf{M}_G^{\text{ext}} \end{bmatrix} \right). \tag{2.32}$$

We choose the geometric center as reference point to obtain more compact generalized contact force directions. Alternatively it is also possible to choose the center of gravity as reference point. For the tippedisk, this parameterization results in much more complex generalized contact force directions.

The virtual displacement $\delta\mathbf{r}_G$ and the virtual rotation $\delta\boldsymbol{\varphi}$ are defined as

$$\delta\mathbf{r}_G := \left.\frac{\partial\hat{\mathbf{r}}_{OG}}{\partial\epsilon}\right|_{\epsilon=\epsilon_0}\delta\epsilon, \qquad \delta\boldsymbol{\varphi} := j^{-1}\left(\hat{\mathbf{R}}^{\mathrm{T}}\frac{\partial\hat{\mathbf{R}}}{\partial\epsilon}\right)\Bigg|_{\epsilon=\epsilon_0}\delta\epsilon \tag{2.33}$$

where $\hat{\mathbf{r}}_{OG}$ and $\hat{\mathbf{R}}$ are introduced as families of curves depending on the variation parameter ϵ. The virtual work (2.32) will set the starting point for the following parameterizations. To remain fully general, we choose as generalized coordinates

$$\mathbf{z} = [{}_I\mathbf{r}_{OG}^{\mathrm{T}},\, R_{11},\, R_{12},\, \ldots,\, R_{33}]^{\mathrm{T}} \in \mathbb{R}^{12}, \tag{2.34}$$

where the 9 components $R_{11}, R_{12}, \ldots, R_{33}$ of the rotation matrix $\mathbf{R}$ depend on the chosen parameterization, e. g., for Euler angles $\boldsymbol{\varphi} = [\alpha,\, \beta,\, \gamma]^{\mathrm{T}} \in \mathbb{R}^3$ as $\mathbf{R}(\boldsymbol{\varphi})$, or $\mathbf{R}(\mathbf{p})$ for quaternions $\mathbf{p} = [p_0,\, p_1,\, p_2,\, p_3]^{\mathrm{T}} \in \mathbb{R}^4$. As generalized velocities we choose

$$\mathbf{v} = [{}_I\mathbf{v}_G^{\mathrm{T}},\, {}_B\boldsymbol{\Omega}^{\mathrm{T}}]^{\mathrm{T}} \in \mathbb{R}^6, \tag{2.35}$$

where ${}_B\boldsymbol{\Omega} = [\omega_x,\, \omega_y,\, \omega_z]^{\mathrm{T}}$ is the angular velocity vector. We express the virtual work of a single rigid body with $\delta\mathbf{s} = \left[{}_I\delta\mathbf{r}_G^{\mathrm{T}},\, {}_B\delta\boldsymbol{\varphi}^{\mathrm{T}}\right]^{\mathrm{T}}$ as

$$\begin{aligned}\delta W = \delta\mathbf{s}^{\mathrm{T}} \Bigg(&\begin{bmatrix} m\,\mathbf{I} & m\,{}_I\tilde{\mathbf{r}}_{GS}^{\mathrm{T}}\mathbf{A}_{IB} \\ m\,{}_B\tilde{\mathbf{r}}_{GS}\mathbf{A}_{IB}^{\mathrm{T}} & {}_B\boldsymbol{\Theta}_G \end{bmatrix} \begin{bmatrix} {}_I\mathbf{a}_P \\ {}_B\boldsymbol{\Psi} \end{bmatrix} \\ &- \begin{bmatrix} -m\,{}_I\boldsymbol{\Omega} \times ({}_I\boldsymbol{\Omega} \times {}_I\mathbf{r}_{GS}) \\ -\,{}_B\boldsymbol{\Omega} \times ({}_B\boldsymbol{\Theta}_G\,{}_B\boldsymbol{\Omega}) \end{bmatrix} - \begin{bmatrix} {}_I\mathbf{F}_G^{\mathrm{ext}} \\ {}_B\mathbf{M}_G^{\mathrm{ext}} \end{bmatrix} \Bigg). \end{aligned} \tag{2.36}$$

This can be written in compact form as

$$\delta W = \delta\mathbf{s}^{\mathrm{T}} \left(\hat{\mathbf{M}}(\mathbf{z})\dot{\mathbf{v}} - \hat{\mathbf{h}}(\mathbf{z}, \mathbf{v}) - \hat{\mathbf{f}}(\mathbf{z}, \mathbf{v}, t) \right) \tag{2.37}$$

with the mass matrix

$$\hat{\mathbf{M}}(\mathbf{z}) = \begin{bmatrix} m\,\mathbf{I} & m\,{}_I\tilde{\mathbf{r}}_{GS}^{\mathrm{T}}\mathbf{A}_{IB} \\ m\,{}_B\tilde{\mathbf{r}}_{GS}\mathbf{A}_{IB}^{\mathrm{T}} & {}_B\boldsymbol{\Theta}_G \end{bmatrix}, \tag{2.38}$$

a vector containing only gyroscopic terms

$$\hat{\mathbf{h}}(\mathbf{z}, \mathbf{v}) = \begin{bmatrix} -m\,{}_I\boldsymbol{\Omega} \times ({}_I\boldsymbol{\Omega} \times {}_I\mathbf{r}_{GS}) \\ -\,{}_B\boldsymbol{\Omega} \times ({}_B\boldsymbol{\Theta}_G\,{}_B\boldsymbol{\Omega}) \end{bmatrix}, \tag{2.39}$$

and the generalized force vector

$$\hat{\mathbf{f}}(\mathbf{z}, \mathbf{v}, t) = \begin{bmatrix} {}_I\mathbf{F}_G^{\mathrm{ext}} \\ {}_B\mathbf{M}_G^{\mathrm{ext}} \end{bmatrix}. \tag{2.40}$$

The dynamical equilibrium is given through the principle of virtual work, which states that the virtual work (2.36) must vanish for all virtual displacements $\delta\mathbf{s}$ at each instant of time t. This leads directly to the equations of motion

$$\hat{\mathbf{M}}(\mathbf{z})\dot{\mathbf{v}} - \hat{\mathbf{h}}(\mathbf{z}, \mathbf{v}) = \hat{\mathbf{f}}(\mathbf{z}, \mathbf{v}, t). \tag{2.41}$$

The relationship ${}_I\dot{\mathbf{r}}_{OG} = {}_I\mathbf{v}_G$ and $\dot{\mathbf{R}} = \mathbf{R}\,j({}_B\boldsymbol{\Omega})$ yield the kinematic equation

$$\dot{\mathbf{z}} = \hat{\mathbf{B}}(\mathbf{z})\mathbf{v}, \tag{2.42}$$

where $\hat{\mathbf{B}}(\mathbf{z}) \in \mathbb{R}^{12\times 6}$ is not given here in full detail. Here, $\mathbf{z}$ has to satisfy the 6 orthogonality conditions $\mathbf{R}^{\mathrm{T}}\mathbf{R} = \mathbf{I}$, which implies that $\hat{\mathbf{B}}(\mathbf{z})$ is such that the velocity constraint $\frac{\mathrm{d}}{\mathrm{d}t}(\mathbf{R}^{\mathrm{T}}\mathbf{R}) = 0$ is fulfilled. With (2.41) and (2.42), we obtain the system in first-order form

$$\begin{aligned} &\hat{\mathbf{M}}(\mathbf{z}, t)\dot{\mathbf{v}} - \hat{\mathbf{h}}(\mathbf{z}, \mathbf{v}, t) = \hat{\mathbf{f}}(\mathbf{z}, \mathbf{v}, t) \\ &\dot{\mathbf{z}} = \hat{\mathbf{B}}(\mathbf{z})\mathbf{v}. \end{aligned} \tag{2.43}$$

In the case of Euler angles the orthogonality condition $\mathbf{R}^{\mathrm{T}}\mathbf{R} = \mathbf{I}$ is always satisfied on position level, such that we do not have to pay attention to an admissible initialization. For a quaternion-based model, the constraint $\mathbf{R}(\mathbf{p})^{\mathrm{T}}\mathbf{R}(\mathbf{p}) = \mathbf{I}$ is fulfilled through the constraint on the norm of the quaternion. The latter, however, is by (2.42) only kept on the velocity level. This implies that the quaternion needs to be properly initialized such that $\mathbf{R}\big(\mathbf{p}(t_0)\big)^{\mathrm{T}}\mathbf{R}\big(\mathbf{p}(t_0)\big) = \mathbf{I}$ holds and that a drift correction may be necessary when (2.43) is simulated numerically.

3. PARAMETERIZATIONS

In the following subsections, we introduce the model in Euler angles and the quaternion-based model to describe the mechanical model of the tippedisk.

3.1. Parameterization: Euler Angles

We parameterize the tippedisk using Euler angles $\boldsymbol{\varphi} = [\alpha,\, \beta,\, \gamma]^{\mathrm{T}}$. We introduce the R-frame with $\mathbf{e}_z^R = \mathbf{e}_z^I$, $\mathbf{e}_x^R = \cos\alpha\, \mathbf{e}_x^I + \sin\alpha\, \mathbf{e}_y^I$ and $\mathbf{e}_y^R = \mathbf{e}_z^R \times \mathbf{e}_x^R$. The sequence of rotation is then given as the first rotation with angle α around the $\mathbf{e}_z^I$-axis, the second rotation with angle β around the $\mathbf{e}_x^R$-axis and the third rotation with angle γ around the $\mathbf{e}_z^G$-axis with corresponding elemental rotations

$$\mathbf{A}_{IR} = \begin{bmatrix} \mathrm{c}\alpha & -\mathrm{s}\alpha & 0 \\ \mathrm{s}\alpha & \mathrm{c}\alpha & 0 \\ 0 & 0 & 1 \end{bmatrix}, \; \mathbf{A}_{RG} = \begin{bmatrix} 1 & 0 & 0 \\ 0 & \mathrm{c}\beta & -\mathrm{s}\beta \\ 0 & \mathrm{s}\beta & \mathrm{c}\beta \end{bmatrix} \text{ and } \mathbf{A}_{GB} = \begin{bmatrix} \mathrm{c}\gamma & -\mathrm{s}\gamma & 0 \\ \mathrm{s}\gamma & \mathrm{c}\gamma & 0 \\ 0 & 0 & 1 \end{bmatrix}, \tag{3.1}$$

where the abbreviations $\mathrm{s}\alpha = \sin(\alpha)$, $\mathrm{c}\alpha = \cos(\alpha)$ etc. have been used. The rotation matrix

$$\mathbf{R}(\boldsymbol{\varphi}) = \begin{bmatrix} \mathrm{c}\alpha\mathrm{c}\gamma - \mathrm{s}\alpha\mathrm{c}\beta\mathrm{s}\gamma & -\mathrm{c}\alpha\mathrm{s}\gamma - \mathrm{s}\alpha\mathrm{c}\beta\mathrm{c}\gamma & \mathrm{s}\alpha\mathrm{s}\beta \\ \mathrm{s}\alpha\mathrm{c}\gamma + \mathrm{c}\alpha\mathrm{c}\beta\mathrm{s}\gamma & -\mathrm{s}\alpha\mathrm{s}\gamma + \mathrm{c}\alpha\mathrm{c}\beta\mathrm{c}\gamma & -\mathrm{c}\alpha\mathrm{s}\beta \\ \mathrm{s}\beta\mathrm{s}\gamma & \mathrm{s}\beta\mathrm{c}\gamma & \mathrm{c}\beta \end{bmatrix}, \tag{3.2}$$

which per se fulfills the orthogonality condition $\mathbf{R}^{\mathrm{T}}\mathbf{R} = \mathbf{I}$. The angular velocity $\boldsymbol{\Omega}$ of the tippedisk expressed in the body-fixed B-frame results from

$${}_B\boldsymbol{\Omega} = \dot{\alpha}\, \mathbf{A}_{RB}^{\mathrm{T}}\, {}_R\mathbf{e}_z^R + \dot{\beta}\, \mathbf{A}_{GB}^{\mathrm{T}}\, {}_G\mathbf{e}_x^G + \dot{\gamma}\, {}_B\mathbf{e}_z^B = \begin{bmatrix} \dot{\alpha}\mathrm{s}\beta\mathrm{s}\gamma + \dot{\beta}\mathrm{c}\gamma \\ \dot{\alpha}\mathrm{s}\beta\mathrm{c}\gamma - \dot{\beta}\mathrm{s}\gamma \\ \dot{\alpha}\mathrm{c}\beta + \dot{\gamma} \end{bmatrix}, \tag{3.3}$$

using $\mathbf{A}_{RB} = \mathbf{A}_{RG}\mathbf{A}_{GB}$. The angular velocity expressed with respect to the I-frame is obtained with $\mathbf{A}_{IB} = \mathbf{R}$ as

$${}_I\boldsymbol{\Omega} = \mathbf{A}_{IB}\, {}_B\boldsymbol{\Omega} = \begin{bmatrix} \dot{\beta}\mathrm{c}\alpha + \dot{\gamma}\mathrm{s}\alpha\mathrm{s}\beta \\ \dot{\beta}\mathrm{s}\alpha - \dot{\gamma}\mathrm{c}\alpha\mathrm{s}\beta \\ \dot{\alpha} + \dot{\gamma}\mathrm{c}\beta \end{bmatrix}. \tag{3.4}$$

The position and the corresponding velocity of the geometric center G are expressed in the inertial I-system as

$${}_I\mathbf{r}_{OG} = \begin{bmatrix} x \\ y \\ z \end{bmatrix} \text{ and } {}_I\mathbf{v}_G = \begin{bmatrix} \dot{x} \\ \dot{y} \\ \dot{z} \end{bmatrix}. \tag{3.5}$$

The gathered coordinates $\mathbf{q} = [x,\, y,\, z,\, \alpha,\, \beta,\, \gamma]^{\mathrm{T}} \in \mathbb{R}^6$ are minimal coordinates for the (free) tippedisk. From (3.3) and (3.5) we obtain the Jacobian matrices of rotation and translation

$${}_B\mathbf{J}_R = \frac{\partial {}_B\boldsymbol{\Omega}}{\partial \dot{\mathbf{q}}} = \begin{bmatrix} 0 & 0 & 0 & \mathrm{s}\beta\mathrm{s}\gamma & \mathrm{c}\gamma & 0 \\ 0 & 0 & 0 & \mathrm{s}\beta\mathrm{c}\gamma & -\mathrm{s}\gamma & 0 \\ 0 & 0 & 0 & \mathrm{c}\beta & 0 & 1 \end{bmatrix}, \; {}_I\mathbf{J}_G = \frac{\partial {}_I\mathbf{v}_G}{\partial \dot{\mathbf{q}}} = \begin{bmatrix} 1 & 0 & 0 & 0 & 0 & 0 \\ 0 & 1 & 0 & 0 & 0 & 0 \\ 0 & 0 & 1 & 0 & 0 & 0 \end{bmatrix}. \tag{3.6}$$

With the two Jacobians ${}_B\mathbf{J}_R$ and ${}_I\mathbf{J}_G$, we obtain the relation

$$\mathbf{v} = \mathbf{A}(\mathbf{q})\,\dot{\mathbf{q}} = \begin{bmatrix} {}_I\mathbf{J}_G \\ {}_B\mathbf{J}_R \end{bmatrix} \dot{\mathbf{q}} \tag{3.7}$$

between the generalized velocities $\mathbf{v} = \left[{}_I\mathbf{v}_G^{\mathrm{T}},\ {}_B\boldsymbol{\Omega}^{\mathrm{T}}\right]^{\mathrm{T}}$ and the time derivative of the generalized position coordinates $\dot{\mathbf{q}}$. Since for nonsingular configurations the linear function ${}_B\boldsymbol{\Omega} = {}_B\boldsymbol{\Omega}(\dot{\boldsymbol{\varphi}})$ is invertible, we find for these situations a properly defined kinematic equation

$$\dot{\mathbf{q}} = \mathbf{B}(\mathbf{q})\mathbf{v}, \quad \text{with} \quad \mathbf{B}(\mathbf{q}) = \mathbf{A}(\mathbf{q})^{-1} \tag{3.8}$$

such that the system (2.43) can be transformed with $\mathbf{z} = \mathbf{z}(\mathbf{q})$ to the new minimal coordinates $\mathbf{q}$:

$$\begin{aligned} &\hat{\mathbf{M}}(\mathbf{z}(\mathbf{q}))\,\dot{\mathbf{v}} - \hat{\mathbf{h}}(\mathbf{z}(\mathbf{q}), \mathbf{v}) = \hat{\mathbf{f}}(\mathbf{z}(\mathbf{q}), \mathbf{v}, t) \\ &\dot{\mathbf{q}} = \mathbf{B}(\mathbf{q})\,\mathbf{v}. \end{aligned} \tag{3.9}$$

The ordinary differential equation (3.9) describes the dynamics of the tippedisk in minimal velocities $\mathbf{v}$ and generalized coordinates $\mathbf{q}$. The transition from minimal velocities $\mathbf{v}$ to the equations of motion in minimal coordinates $\mathbf{q}$ leads with the regular transformation

$$\mathbf{v} = \mathbf{v}(\mathbf{q}, \dot{\mathbf{q}}) = \mathbf{B}(\mathbf{q})^{-1}\dot{\mathbf{q}} = \mathbf{A}(\mathbf{q})\dot{\mathbf{q}} \tag{3.10}$$

to the Lagrangian system of the form

$$\mathbf{M}(\mathbf{q})\,\ddot{\mathbf{q}} - \mathbf{h}(\mathbf{q}, \dot{\mathbf{q}}) = \mathbf{f}(\mathbf{q}, \dot{\mathbf{q}}, t). \tag{3.11}$$

Equation (3.11) defines the equations of motion for generalized coordinates $\mathbf{q}$, where $\mathbf{M}$ describes the mass matrix and $\mathbf{h}$ a vector containing all inertia forces which are not linear in the generalized accelerations $\ddot{\mathbf{q}}$, i. e., gyroscopic forces. The mass matrix and the vector of gyroscopic forces are given as

$$\mathbf{M}(\mathbf{q}) := \mathbf{A}(\mathbf{q})^{\mathrm{T}}\,\hat{\mathbf{M}}\big(\mathbf{z}(\mathbf{q})\big)\,\mathbf{A}(\mathbf{q}) = \begin{bmatrix} \mathbf{M}_{11} & \mathbf{M}_{12} \\ \mathbf{M}_{21} & \mathbf{M}_{22} \end{bmatrix} \tag{3.12}$$

with

$$\begin{aligned} \mathbf{M}_{11} &= \begin{bmatrix} m & 0 & 0 \\ 0 & m & 0 \\ 0 & 0 & m \end{bmatrix}, \quad \mathbf{M}_{21} = \mathbf{M}_{12}^{\mathrm{T}} \\ \mathbf{M}_{12} &= me \begin{bmatrix} -\mathrm{c}\alpha\mathrm{c}\beta\mathrm{s}\gamma - \mathrm{s}\alpha\mathrm{c}\gamma & \mathrm{s}\alpha\mathrm{s}\beta\mathrm{s}\gamma & -\mathrm{c}\alpha\mathrm{s}\gamma - \mathrm{s}\alpha\mathrm{c}\beta\mathrm{c}\gamma \\ -\mathrm{s}\alpha\mathrm{c}\beta\mathrm{s}\gamma + \mathrm{c}\alpha\mathrm{c}\gamma & -\mathrm{c}\alpha\mathrm{s}\beta\mathrm{s}\gamma & -\mathrm{s}\alpha\mathrm{s}\gamma + \mathrm{c}\alpha\mathrm{c}\beta\mathrm{c}\gamma \\ 0 & \mathrm{c}\beta\mathrm{s}\gamma & \mathrm{s}\beta\mathrm{c}\gamma \end{bmatrix} \\ \mathbf{M}_{22} &= \begin{bmatrix} (A\mathrm{s}^2\gamma + B\mathrm{c}^2\gamma)\mathrm{s}^2\beta + Cc^2\beta & (A-B)\mathrm{s}\beta\mathrm{s}\gamma\mathrm{c}\gamma & C\mathrm{c}\beta \\ (A-B)\mathrm{s}\beta\mathrm{s}\gamma\mathrm{c}\gamma & A\mathrm{c}^2\gamma + B\mathrm{s}^2\gamma & 0 \\ C\mathrm{c}\beta & 0 & C \end{bmatrix} \end{aligned} \tag{3.13}$$

and

$$\begin{aligned} \mathbf{h}(\mathbf{q}, \dot{\mathbf{q}}) :&= \mathbf{A}(\mathbf{q})^{\mathrm{T}} \left(\hat{\mathbf{h}}\left(\mathbf{z}(\mathbf{q}), \mathbf{A}(\mathbf{q})\dot{\mathbf{q}}, t\right) - \hat{\mathbf{M}}(\mathbf{z}(\mathbf{q}), t)\,\dot{\mathbf{A}}(\mathbf{q})\dot{\mathbf{q}}\right) \\ &= \begin{bmatrix} h_1 & h_2 & h_3 & h_4 & h_5 & h_6 \end{bmatrix}^{\mathrm{T}} \end{aligned} \tag{3.14}$$

with

$$h_1 = me\left[\dot\alpha^2(\mathrm{c}\alpha\mathrm{c}\gamma - \mathrm{s}\alpha\mathrm{c}\beta\mathrm{s}\gamma) - \dot\beta^2\mathrm{s}\alpha\mathrm{c}\beta\mathrm{s}\gamma + \dot\gamma^2(\mathrm{c}\alpha\mathrm{c}\gamma - \mathrm{s}\alpha\mathrm{c}\beta\mathrm{s}\gamma)\right.$$
$$\left. - 2\dot\alpha\dot\beta\mathrm{c}\alpha\mathrm{s}\beta\mathrm{s}\gamma - 2\dot\alpha\dot\gamma(\mathrm{s}\alpha\mathrm{s}\gamma - \mathrm{c}\alpha\mathrm{c}\beta\mathrm{c}\gamma) - 2\dot\beta\dot\gamma\mathrm{s}\alpha\mathrm{s}\beta\mathrm{c}\gamma\right], \tag{3.15}$$

$$h_2 = me\left[\dot\alpha^2(\mathrm{s}\alpha\mathrm{c}\gamma + \mathrm{c}\alpha\mathrm{c}\beta\mathrm{s}\gamma) + \dot\beta^2\mathrm{c}\alpha\mathrm{c}\beta\mathrm{s}\gamma + \dot\gamma^2(\mathrm{s}\alpha\mathrm{c}\gamma + \mathrm{c}\alpha\mathrm{c}\beta\mathrm{s}\gamma)\right.$$
$$\left. - 2\dot\alpha\dot\beta\mathrm{s}\alpha\mathrm{s}\beta\mathrm{s}\gamma + 2\dot\alpha\dot\gamma(\mathrm{c}\alpha\mathrm{s}\gamma + \mathrm{s}\alpha\mathrm{c}\beta\mathrm{c}\gamma) + 2\dot\beta\dot\gamma\mathrm{c}\alpha\mathrm{s}\beta\mathrm{c}\gamma\right], \tag{3.16}$$

$$h_3 = me\left[\dot\beta^2\mathrm{s}\beta\mathrm{s}\gamma + \dot\gamma^2\mathrm{s}\beta\mathrm{s}\gamma - 2\dot\beta\dot\gamma\mathrm{c}\beta\mathrm{c}\gamma\right], \tag{3.17}$$

$$h_4 = -\dot\beta^2(A-B)\mathrm{c}\beta\mathrm{s}\gamma\mathrm{c}\gamma - 2\dot\alpha\dot\beta(A\mathrm{s}^2\gamma + B\mathrm{c}^2\gamma - C)\mathrm{s}\beta\mathrm{c}\beta$$
$$- 2\dot\alpha\dot\gamma(A-B)\mathrm{s}^2\beta\mathrm{s}\gamma\mathrm{c}\gamma - \dot\beta\dot\gamma\mathrm{s}\beta\big[(A-B)(\mathrm{c}^2\gamma - \mathrm{s}^2\gamma) - C\big], \tag{3.18}$$

$$h_5 = \dot\alpha^2\mathrm{s}\beta\mathrm{c}\beta(A\mathrm{s}^2\gamma + B\mathrm{c}^2\gamma - C) - \dot\alpha\dot\gamma\mathrm{s}\beta\big[(A-B)(\mathrm{c}^2\gamma - \mathrm{s}^2\gamma) + C\big] + 2\dot\beta\dot\gamma(A-B)\mathrm{s}\gamma\mathrm{c}\gamma, \tag{3.19}$$

$$h_6 = \dot\alpha^2(A-B)\mathrm{s}^2\beta\mathrm{s}\gamma\mathrm{c}\gamma - \dot\beta^2\mathrm{s}\gamma\mathrm{c}\gamma(A-B) + \dot\alpha\dot\beta\mathrm{s}\beta\big[(A-B)(\mathrm{c}^2\gamma - \mathrm{s}^2\gamma) + C\big]. \tag{3.20}$$

With Eqs. (3.12)–(3.20) the left-hand side of the equations of motion (3.11) and therefore all inertia forces are determined. The right-hand side will not be transformed, since the generalized force directions of external forces $\mathbf{F}^{\mathrm{ext}}$ can directly be extracted from the corresponding Jacobians. It contains all noninertial forces such as gravitational, normal contact and friction forces. To take gravitational forces into account, we express the position of the center of gravity S as

$${}_I\mathbf{r}_{OS} = {}_I\mathbf{r}_{OG} + e\,{}_I\mathbf{e}_x^B = \begin{bmatrix} x + e(\mathrm{c}\alpha\mathrm{c}\gamma - \mathrm{s}\alpha\mathrm{c}\beta\mathrm{s}\gamma) \\ y + e(\mathrm{s}\alpha\mathrm{c}\gamma + \mathrm{c}\alpha\mathrm{c}\beta\mathrm{s}\gamma) \\ z + e\mathrm{s}\beta\mathrm{s}\gamma \end{bmatrix}. \tag{3.21}$$

The time derivative leads to the velocity

$${}_I\mathbf{v}_S = \begin{bmatrix} \dot x - e\big[\dot\alpha(\mathrm{s}\alpha\mathrm{c}\gamma + \mathrm{c}\alpha\mathrm{c}\beta\mathrm{s}\gamma) - \dot\beta\mathrm{s}\alpha\mathrm{s}\beta\mathrm{s}\gamma + \dot\gamma(\mathrm{c}\alpha\mathrm{s}\gamma + \mathrm{s}\alpha\mathrm{c}\beta\mathrm{c}\gamma)\big] \\ \dot y + e\big[\dot\alpha(\mathrm{c}\alpha\mathrm{c}\gamma - \mathrm{s}\alpha\mathrm{c}\beta\mathrm{s}\gamma) - \dot\beta\mathrm{c}\alpha\mathrm{s}\beta\mathrm{s}\gamma - \dot\gamma(\mathrm{s}\alpha\mathrm{s}\gamma - \mathrm{c}\alpha\mathrm{c}\beta\mathrm{c}\gamma)\big] \\ \dot z + e(\dot\beta\mathrm{c}\beta\mathrm{s}\gamma + \dot\gamma\mathrm{s}\beta\mathrm{c}\gamma) \end{bmatrix}, \tag{3.22}$$

from which we can extract the Jacobian matrix

$${}_I\mathbf{J}_S = \left[\begin{array}{c|ccc} & -e(\mathrm{s}\alpha\mathrm{c}\gamma + \mathrm{c}\alpha\mathrm{c}\beta\mathrm{s}\gamma) & e\mathrm{s}\alpha\mathrm{s}\beta\mathrm{s}\gamma & -e(\mathrm{c}\alpha\mathrm{s}\gamma + \mathrm{s}\alpha\mathrm{c}\beta\mathrm{c}\gamma) \\ \mathbf{I} & e(\mathrm{c}\alpha\mathrm{c}\gamma - \mathrm{s}\alpha\mathrm{c}\beta\mathrm{s}\gamma) & -e\mathrm{c}\alpha\mathrm{s}\beta\mathrm{s}\gamma & -e(\mathrm{s}\alpha\mathrm{s}\gamma - \mathrm{c}\alpha\mathrm{c}\beta\mathrm{c}\gamma) \\ & 0 & e\mathrm{c}\beta\mathrm{s}\gamma & e\mathrm{s}\beta\mathrm{c}\gamma \end{array}\right] \tag{3.23}$$

of the center of gravity. Hence, the projected generalized force of gravitational force ${}_I\mathbf{F}_g = [0,\, 0,\, -mg]^{\mathrm{T}}$ follows from (3.23) as

$$\mathbf{f}_g = {}_I\mathbf{J}_S^{\mathrm{T}}\,{}_I\mathbf{F}_g = -mg\begin{bmatrix} 0 & 0 & 1 & 0 & e\mathrm{c}\beta\mathrm{s}\gamma & e\mathrm{s}\beta\mathrm{c}\gamma \end{bmatrix}^{\mathrm{T}}. \tag{3.24}$$

Using (2.10) together with the rigid body formula (2.13), the velocity of the contact point C_1 follows as

$${}_I\mathbf{v}_{C_1} = {}_I\mathbf{v}_G + {}_I\boldsymbol{\Omega} \times {}_I\mathbf{r}_{GC_1} = \begin{bmatrix} \dot x + r(\dot\alpha\mathrm{c}\alpha\mathrm{c}\beta - \dot\beta\mathrm{s}\alpha\mathrm{s}\beta + \dot\gamma\mathrm{c}\alpha) \\ \dot y + r(\dot\alpha\mathrm{s}\alpha\mathrm{c}\beta + \dot\beta\mathrm{c}\alpha\mathrm{s}\beta + \dot\gamma\mathrm{s}\alpha) \\ \dot z - r\dot\beta\mathrm{c}\beta \end{bmatrix}. \tag{3.25}$$

Since the support is not moving, the velocity ${}_I\mathbf{v}_{C_1}$ is equivalent to the relative contact velocity of the contact point C_1. The components of ${}_I\mathbf{v}_{C_1}$ can be split according to (2.14) and (2.15) into the

normal relative velocity

$$\gamma_{N_1} = \dot{z} - r\dot{\beta}\mathrm{c}\beta \tag{3.26}$$

and into the sliding velocity

$$\boldsymbol{\gamma}_{T_1} = \begin{bmatrix} \dot{x} + r(\dot{\alpha}\mathrm{c}\alpha\mathrm{c}\beta - \dot{\beta}\mathrm{s}\alpha\mathrm{s}\beta + \dot{\gamma}\mathrm{c}\alpha) \\ \dot{y} + r(\dot{\alpha}\mathrm{s}\alpha\mathrm{c}\beta + \dot{\beta}\mathrm{c}\alpha\mathrm{s}\beta + \dot{\gamma}\mathrm{s}\alpha) \end{bmatrix}. \tag{3.27}$$

The corresponding generalized normal force direction $\mathbf{w}_{N_1}$ is obtained from (3.26) as

$$\mathbf{w}_{N_1} = \left(\frac{\partial \gamma_{N_1}}{\partial \dot{\mathbf{q}}}\right)^{\mathrm{T}} = \begin{bmatrix} 0 & 0 & 1 & 0 & -r\mathrm{c}\beta & 0 \end{bmatrix}^{\mathrm{T}} \in \mathbb{R}^{6\times 1}, \tag{3.28}$$

whereas (3.27) provides the generalized force directions

$$\mathbf{W}_{T_1} = \left(\frac{\partial \boldsymbol{\gamma}_{T_1}}{\partial \dot{\mathbf{q}}}\right)^{\mathrm{T}} = \begin{bmatrix} 1 & 0 & 0 & r\mathrm{c}\alpha\mathrm{c}\beta & -r\mathrm{s}\alpha\mathrm{s}\beta & r\mathrm{c}\alpha \\ 0 & 1 & 0 & r\mathrm{s}\alpha\mathrm{c}\beta & r\mathrm{c}\alpha\mathrm{s}\beta & r\mathrm{s}\alpha \end{bmatrix}^{\mathrm{T}} \in \mathbb{R}^{6\times 2}, \tag{3.29}$$

for the tangential friction forces. The generalized normal and tangential force directions for the contact points C_2 and C_3 can be calculated analogously using Eq. (2.11). Finally, the contact force directions can be collected in generalized normal force directions

$$\mathbf{W}_N = \begin{bmatrix} \mathbf{w}_{N_1} & \mathbf{w}_{N_2} & \mathbf{w}_{N_3} \end{bmatrix} \in \mathbb{R}^{6\times 3} \tag{3.30}$$

and generalized tangential force directions

$$\mathbf{W}_T = \begin{bmatrix} \mathbf{W}_{T_1} & \mathbf{W}_{T_2} & \mathbf{W}_{T_3} \end{bmatrix} \in \mathbb{R}^{6\times 6}. \tag{3.31}$$

To describe pivoting friction, we use the relative spin velocity ω_{IB} and the contact radius ε_i to calculate the relative pivoting velocity as

$$\gamma_{\tau_i} := \varepsilon_i\, \omega_{IB}. \tag{3.32}$$

Pivoting friction can be regarded separately or by using Coulomb – Contensou friction. The generalized pivoting friction force direction for one contact point C_i is then given as

$$\mathbf{w}_{\tau_i} = \left(\frac{\partial \gamma_{\tau_i}}{\partial \dot{\mathbf{q}}}\right)^{\mathrm{T}} = \varepsilon_i \begin{bmatrix} 0 & 0 & 0 & 1 & 0 & \cos(\beta) \end{bmatrix}^{\mathrm{T}} \in \mathbb{R}^{6\times 1} \tag{3.33}$$

and can be gathered as $\mathbf{W}_\tau = \begin{bmatrix} \mathbf{w}_{\tau_1} & \mathbf{w}_{\tau_2} & \mathbf{w}_{\tau_3} \end{bmatrix} \in \mathbb{R}^{6\times 3}$. The relative velocity γ_R of the contact point C_i with respect to its body-fixed point is defined in (2.17). Since we choose Euler angles, this velocity is directly given as a function

$$\gamma_{R_i} = -r\dot{\varphi} = -r\dot{\gamma}, \tag{3.34}$$

only depending on generalized velocities $\dot{\mathbf{q}}$, such that the generalized force direction

$$\mathbf{w}_{R_i} = r \begin{bmatrix} 0 & 0 & 0 & 0 & 0 & -1 \end{bmatrix}^{\mathrm{T}} \in \mathbb{R}^{6\times 1} \tag{3.35}$$

follows. For an inclined disk, such that there exists a unique contact point with minimal height, the generalized force direction for contour friction is given as

$$\mathbf{W}_R = r \begin{bmatrix} 0 & 0 & 0 & 0 & 0 & -1 \\ 0 & 0 & 0 & 0 & 0 & 0 \\ 0 & 0 & 0 & 0 & 0 & 0 \end{bmatrix}^{\mathrm{T}} \in \mathbb{R}^{6\times 3}. \tag{3.36}$$

At this point we mention that the generalized force direction $\mathbf{W}_R$ should be adapted for a horizontally orientated disk. As this horizontal configuration is intrinsically equal to the singularity of the Euler angles and leads to a singular mass matrix [11], it is sufficient to consider $\mathbf{W}_R$ for

the inclined tippedisk. As will be seen, this singularity does not play a role during the inversion phenomenon.

Together with the kinetic quantities, i. e., mass matrix $\mathbf{M}$, the vector of gyroscopic forces $\mathbf{h}$, the gravitational force $\mathbf{f}_g$ from (3.12), (3.14), (3.24), and the generalized force directions from (3.30)–(3.36), we obtain the equations of motion

$$\mathbf{M}(\mathbf{q})\ddot{\mathbf{q}} - \mathbf{h}(\mathbf{q},\dot{\mathbf{q}}) = \mathbf{f}_g + \mathbf{W}_N\boldsymbol{\lambda}_N + \mathbf{W}_T\boldsymbol{\lambda}_T + \mathbf{W}_\tau\boldsymbol{\lambda}_\tau + \mathbf{W}_R\boldsymbol{\lambda}_R, \tag{3.37}$$

which can also be written in compact form as

$$\mathbf{M}(\mathbf{q})\ddot{\mathbf{q}} - \mathbf{h}(\mathbf{q},\dot{\mathbf{q}}) = \mathbf{f}_g + \mathbf{W}\boldsymbol{\lambda} \tag{3.38}$$

with $\mathbf{W} = [\mathbf{W}_N,\, \mathbf{W}_T,\, \mathbf{W}_\tau,\, \mathbf{W}_R]$ and $\boldsymbol{\lambda} = \left[\boldsymbol{\lambda}_N^{\mathrm{T}},\, \boldsymbol{\lambda}_T^{\mathrm{T}},\, \boldsymbol{\lambda}_\tau^{\mathrm{T}},\, \boldsymbol{\lambda}_R^{\mathrm{T}}\right]^{\mathrm{T}}$. Introducing the kinematic relationship $\dot{\mathbf{q}} = \mathbf{u}$, or more formal $\dot{\mathbf{q}} = \mathbf{F}(\mathbf{q})\mathbf{u}$ with $\mathbf{F}(\mathbf{q}) = \mathbf{I}$ (for a unified numerical treatment), the system (3.38) can be written in first-order form as

$$\begin{aligned} \mathbf{M}(\mathbf{q})\dot{\mathbf{u}} - \mathbf{h}(\mathbf{q},\mathbf{u}) &= \mathbf{f}_g + \mathbf{W}\boldsymbol{\lambda} \\ \dot{\mathbf{q}} &= \mathbf{F}(\mathbf{q})\mathbf{u}. \end{aligned} \tag{3.39}$$

3.2. Parameterization: Quaternions

In the second approach, the rotation matrix $\mathbf{R}$ is parameterized using unit quaternions $\mathbf{p} = [p_0,\, p_1,\, p_2,\, p_3]^{\mathrm{T}} \in \mathbb{R}^4$, with $\|\mathbf{p}\|_4 = 1$. The expression $\|.\|_4$ denotes the Euclidean norm in $\mathbb{R}^4$. The rotation matrix $\mathbf{R}$ then can be parameterized as

$$\mathbf{R}(\mathbf{p}) = \begin{bmatrix} 2(p_0^2+p_1^2)-1 & 2(p_1p_2-p_0p_3) & 2(p_1p_3+p_0p_2) \\ 2(p_1p_2+p_0p_3) & 2(p_0^2+p_2^2)-1 & 2(p_2p_3-p_0p_1) \\ 2(p_1p_3-p_0p_2) & 2(p_2p_3+p_0p_1) & 2(p_0^2+p_3^2)-1 \end{bmatrix}, \tag{3.40}$$

which fulfills the orthogonality condition $\mathbf{R}^{\mathrm{T}}\mathbf{R} = \mathbf{I}$ if $\mathbf{p}$ is a unit quaternion. We use the same parameterization for the position $\mathbf{r}_{OG}$ of the reference point G as in Euler angles, (3.5). As generalized coordinates $\mathbf{q}$ and minimal velocities $\mathbf{u}$ we choose

$$\mathbf{q} := \begin{bmatrix} {}_I\mathbf{r}_{OG}^{\mathrm{T}} & \mathbf{p}^{\mathrm{T}} \end{bmatrix}^{\mathrm{T}} = \begin{bmatrix} x & y & z & p_0 & p_2 & p_2 & p_3 \end{bmatrix}^{\mathrm{T}} \in \mathbb{R}^7 \tag{3.41}$$

and

$$\mathbf{u} := \begin{bmatrix} \dot{x} & \dot{y} & \dot{z} & \omega_x & \omega_y & \omega_z \end{bmatrix}^{\mathrm{T}} \in \mathbb{R}^6, \tag{3.42}$$

such that the angular velocity $\boldsymbol{\Omega}$ of the tippedisk expressed in the body-fixed B-frame results as

$${}_B\boldsymbol{\Omega} =: \begin{bmatrix} \omega_x & \omega_y & \omega_z \end{bmatrix}^{\mathrm{T}}. \tag{3.43}$$

The linear kinematic equation $\dot{\mathbf{q}} = \mathbf{F}(\mathbf{q})\mathbf{u}$ can be obtained using the time derivative of $\|\mathbf{p}\|_4^2 = \mathbf{p}^{\mathrm{T}}\mathbf{p} = 1$ as

$$\dot{\mathbf{q}} = \mathbf{F}(\mathbf{q})\mathbf{u} = \begin{bmatrix} \mathbf{I} & \mathbf{0} \\ \mathbf{0} & \frac{1}{2}\bar{\mathbf{H}}^{\mathrm{T}} \end{bmatrix} \mathbf{u}. \tag{3.44}$$

Similar to [24], we obtain

$$\bar{\mathbf{H}}^{\mathrm{T}} = \begin{bmatrix} -p_1 & -p_2 & -p_3 \\ p_0 & -p_3 & p_2 \\ p_3 & p_0 & -p_1 \\ -p_2 & p_1 & p_0 \end{bmatrix}. \tag{3.45}$$

From (3.5) and (3.43), the Jacobian matrices follow as

$$ {}_I\mathbf{J}_G = \begin{bmatrix} 1 & 0 & 0 & 0 & 0 & 0 \\ 0 & 1 & 0 & 0 & 0 & 0 \\ 0 & 0 & 1 & 0 & 0 & 0 \end{bmatrix} \quad \text{and} \quad {}_B\mathbf{J}_R = \begin{bmatrix} 0 & 0 & 0 & 1 & 0 & 0 \\ 0 & 0 & 0 & 0 & 1 & 0 \\ 0 & 0 & 0 & 0 & 0 & 1 \end{bmatrix}. \tag{3.46} $$

Inserting $\mathbf{A}_{IB} = \mathbf{R}(\mathbf{p})$ into (2.43), we obtain with $\mathbf{v} = \mathbf{u}$ the equations of motions

$$ \mathbf{M}(\mathbf{q})\dot{\mathbf{u}} - \mathbf{h}(\mathbf{q}, \mathbf{u}) = \mathbf{f}(\mathbf{q}, \mathbf{u}) \tag{3.47} $$

with the mass matrix

$$ \mathbf{M}(\mathbf{q}) = \begin{bmatrix} m\,\mathbf{I} & m\,{}_I\tilde{\mathbf{r}}_{GS}^{\mathrm{T}}\mathbf{R}(\mathbf{p}) \\ m\,{}_B\tilde{\mathbf{r}}_{GS}\mathbf{R}^{\mathrm{T}}(\mathbf{p}) & {}_B\boldsymbol{\Theta}_G \end{bmatrix}, \tag{3.48} $$

and with ${}_I\boldsymbol{\Omega} = \mathbf{R}(\mathbf{p})\,{}_B\boldsymbol{\Omega}$ the vector of gyroscopic forces

$$ \mathbf{h}(\mathbf{q}, \mathbf{u}) = \begin{bmatrix} -m\,{}_I\boldsymbol{\Omega} \times ({}_I\boldsymbol{\Omega} \times {}_I\mathbf{r}_{GS}) \\ -{}_B\boldsymbol{\Omega} \times ({}_B\boldsymbol{\Theta}_G\,{}_B\boldsymbol{\Omega}) \end{bmatrix}. \tag{3.49} $$

Equations (3.48) and (3.49) define the left-hand side of (3.47). To determine the right-hand side, we have to take gravitational and contact forces into account. The gravitational force ${}_I\mathbf{F}_g = [0,\, 0,\, -mg]^{\mathrm{T}}$ is applied at the center of gravity S. The velocity of S can be determined using the rigid body formula (2.13)

$$ {}_I\mathbf{v}_S = {}_I\mathbf{v}_G - {}_I\mathbf{r}_{GS} \times {}_I\boldsymbol{\Omega} = {}_I\mathbf{v}_G - {}_I\tilde{\mathbf{r}}_{GS}\,\mathbf{R}_B\boldsymbol{\Omega}, \tag{3.50} $$

from which we extract the Jacobian

$$ {}_I\mathbf{J}_S = \begin{bmatrix} \mathbf{I} & {}_I\mathbf{r}_{GS}^{\mathrm{T}}\mathbf{R} \end{bmatrix}, \tag{3.51} $$

which we use to obtain the generalized gravitational force

$$ \mathbf{f}_g = {}_I\mathbf{J}_S^{\mathrm{T}}\,{}_I\mathbf{F}_g. \tag{3.52} $$

Similarly, we calculate the Jacobians of all contact points, using again the rigid body formula

$$ {}_I\mathbf{v}_{C_i} = {}_I\mathbf{v}_G - {}_I\mathbf{r}_{GC_i} \times {}_I\boldsymbol{\Omega} = \begin{bmatrix} \mathbf{I} & {}_I\tilde{\mathbf{r}}_{GC_i}^{\mathrm{T}}\mathbf{R} \end{bmatrix}\mathbf{u}. \tag{3.53} $$

From (3.53), the Jacobian

$$ {}_I\mathbf{J}_{C_i} = \begin{bmatrix} \mathbf{I} & {}_I\tilde{\mathbf{r}}_{GC_i}^{\mathrm{T}}\mathbf{R} \end{bmatrix} \tag{3.54} $$

can be extracted. The generalized force directions of the normal and tangential contact forces are then given as the projections onto the $\mathbf{e}_x^I$-, $\mathbf{e}_y^I$- and $\mathbf{e}_z^I$-axis. For a single contact point C_i, the generalized normal force direction is obtained as

$$ \mathbf{w}_{N_i} = \begin{bmatrix} ({}_I\mathbf{e}_z^I)^{\mathrm{T}} & -({}_I\mathbf{e}_z^I)^{\mathrm{T}}\,{}_I\tilde{\mathbf{r}}_{GC_i}\mathbf{R} \end{bmatrix}^{\mathrm{T}} \in \mathbb{R}^{6\times 1} \tag{3.55} $$

and the generalized tangential force direction as

$$ \mathbf{W}_{T_i} = \begin{bmatrix} ({}_I\mathbf{e}_x^I)^{\mathrm{T}} & -({}_I\mathbf{e}_x^I)^{\mathrm{T}}\,{}_I\tilde{\mathbf{r}}_{GC_i}\mathbf{R} \\ ({}_I\mathbf{e}_y^I)^{\mathrm{T}} & -({}_I\mathbf{e}_y^I)^{\mathrm{T}}\,{}_I\tilde{\mathbf{r}}_{GC_i}\mathbf{R} \end{bmatrix}^{\mathrm{T}} \in \mathbb{R}^{6\times 2}. \tag{3.56} $$

These force directions of forces acting in C_i can be gathered in matrices

$$ \mathbf{W}_N = \begin{bmatrix} \mathbf{w}_{N_1} & \mathbf{w}_{N_2} & \mathbf{w}_{N_3} \end{bmatrix} \in \mathbb{R}^{6\times 3} \tag{3.57} $$

and

$$ \mathbf{W}_T = \begin{bmatrix} \mathbf{W}_{T_1} & \mathbf{W}_{T_2} & \mathbf{W}_{T_3} \end{bmatrix} \in \mathbb{R}^{6\times 6}. \tag{3.58} $$

To obtain the generalized force directions of pivoting and contour frictional forces, we take the relative spin velocity

$$\omega_{IB} := ({}_I\mathbf{e}_z^I)^{\mathrm{T}}\, {}_I\boldsymbol{\Omega} = ({}_I\mathbf{e}_z^I)^{\mathrm{T}}\, \mathbf{R}_B \boldsymbol{\Omega}, \tag{3.59}$$

from which the relative gap velocities

$$\gamma_{\tau_i} := \varepsilon_i\, \omega_{IB} \tag{3.60}$$

follow for each contact point. Together with the rotational Jacobian ${}_B\mathbf{J}_R$, we identify the linear part in $\mathbf{u}$, which is equivalent to the generalized force direction

$$\mathbf{w}_{\tau_i} = \varepsilon_i \begin{bmatrix} 0 & 0 & 0 & ({}_I\mathbf{e}_z^I)^{\mathrm{T}}\, \mathbf{R} \end{bmatrix}^{\mathrm{T}} \in \mathbb{R}^{6\times 1}, \tag{3.61}$$

with the associated contact radii ε_i. The generalized force direction for pivoting friction of all contact points results as

$$\mathbf{W}_\tau = \begin{bmatrix} \mathbf{w}_{\tau_1} & \mathbf{w}_{\tau_2} & \mathbf{w}_{\tau_3} \end{bmatrix} \in \mathbb{R}^{6\times 3}. \tag{3.62}$$

To consider contour friction, we use (2.17)

$$\gamma_{R_i} = -r\dot{\varphi}, \tag{3.63}$$

which is equivalent to the contour velocity in Euler angles (3.34). Using the horizontality condition $\mathbf{e}_x^G \cdot \mathbf{e}_z^I \equiv 0$, we obtain

$$\dot{\varphi} = \begin{bmatrix} \frac{R_{31}R_{33}}{R_{31}^2+R_{32}^2} & \frac{R_{32}R_{33}}{R_{31}^2+R_{32}^2} & 1 \end{bmatrix} {}_B\tilde{\mathbf{J}}_R\, \mathbf{u}, \tag{3.64}$$

such that the generalized force direction for contour friction of the contact point C_1 is defined as

$$\mathbf{w}_{R_1} = -r \begin{bmatrix} \frac{R_{31}R_{33}}{R_{31}^2+R_{32}^2} & \frac{R_{32}R_{33}}{R_{31}^2+R_{32}^2} & 1 \end{bmatrix} {}_B\tilde{\mathbf{J}}_R \in \mathbb{R}^{6\times 1}. \tag{3.65}$$

Since the definition of the contact point C_1 is only valid for nonhorizontal configurations, the generalized force direction for contour friction is given as

$$\mathbf{W}_R = -r \begin{bmatrix} 0 & 0 & 0 & \frac{R_{31}R_{33}}{R_{31}^2+R_{32}^2} & \frac{R_{32}R_{33}}{R_{31}^2+R_{32}^2} & 1 \\ 0 & 0 & 0 & 0 & 0 & 0 \\ 0 & 0 & 0 & 0 & 0 & 0 \end{bmatrix}^{\mathrm{T}} \in \mathbb{R}^{6\times 3}. \tag{3.66}$$

For a horizontally orientated disk, these contact points C_i are not properly defined [15]. The generalized force direction then follows as $\mathbf{W}_R = \mathbf{0} \in \mathbb{R}^{6\times 3}$.

As the quaternion-based model is already written in first-order form, we collect the generalized force directions $\mathbf{W} = [\mathbf{W}_N, \mathbf{W}_T, \mathbf{W}_\tau, \mathbf{W}_R]$ and $\boldsymbol{\lambda} = \left[\boldsymbol{\lambda}_N^{\mathrm{T}}, \boldsymbol{\lambda}_T^{\mathrm{T}}, \boldsymbol{\lambda}_\tau^{\mathrm{T}}, \boldsymbol{\lambda}_R^{\mathrm{T}}\right]^{\mathrm{T}}$, such that the system equations can be written as

$$\begin{aligned} &\mathbf{M}(\mathbf{q})\dot{\mathbf{u}} - \mathbf{h}(\mathbf{q},\mathbf{u}) = \mathbf{f}_g + \mathbf{W}\boldsymbol{\lambda}, \\ &\dot{\mathbf{q}} = \mathbf{F}(\mathbf{q})\mathbf{u} \end{aligned} \tag{3.67}$$

using the mass matrix $\mathbf{M}$ from (3.48), the vector of gyroscopic forces $\mathbf{h}$ from (3.49) together with the generalized gravitational force $\mathbf{f}_g$ from (3.52) and the kinematic equation from (3.44). The equation of motion together with the kinematic equation in Eq. (3.67) only fulfills the quaternion constraint on velocity level. To prevent this constraint from drifting, the quaternion has to be normalized after each time step. This correction is only needed in a numerical scheme as the exact solution of Eq. (3.67) does not need a Lagrange multiplier.

4. NONSMOOTH AND SMOOTH NUMERICS

Moreau's time-stepping scheme is a numerical simulation method for multibody systems with frictional unilateral constraints which falls under the class of velocity-impulse based integration methods. The scheme may be derived from a direct discretization of an equality of measures, incorporating the equation of motion and the impact equation, together with a discrete approximation of the combined contact and impact laws. Here, we will only briefly present the final stepping equations, taking care to explain how the sophisticated contact laws are treated, and refer the reader to [1, 10, 18, 23] for a detailed discussion of the scheme.

We use an equidistant grid $t_0 < t_1 < \ldots < t_i < t_{i+1} < \ldots < t_{\text{final}}$ with $t_{i+1} - t_i = \Delta t$ on which we search for approximants $\mathbf{q}_i \approx \mathbf{q}(t_i)$ and $\mathbf{u}_i \approx \mathbf{u}(t_i)$. Using the notation A for the beginning of the time step and E for the end of the time step, we present the scheme to calculate from known positions $\mathbf{q}_A := \mathbf{q}_i$ and velocities $\mathbf{u}_A := \mathbf{u}_i$ the new quantities $\mathbf{q}_E := \mathbf{q}_{i+1}$ and $\mathbf{u}_E := \mathbf{u}_{i+1}$.

Moreau's time-stepping scheme:

1) Calculate the midpoint $t_M = t_A + \frac{1}{2}(t_E - t_A) = t_A + \frac{1}{2}\Delta t$

2) Approximate the midpoint position at time t_M using a forward Euler step: $\mathbf{q}_M = \mathbf{q}_A + \frac{1}{2}\mathbf{F}(\mathbf{q}_A)\mathbf{u}_A\,\Delta t$

3) Evaluate the mass matrix $\mathbf{M}_M := \mathbf{M}(\mathbf{q}_M)$, generalized force directions $\mathbf{W}_{*M} := \mathbf{W}_*(\mathbf{q}_M)$, the vector of gyroscopic forces $\mathbf{h}_M := \mathbf{h}(\mathbf{q}_M, \mathbf{u}_A)$ and $\mathbf{f}_{g,M} := \mathbf{f}_g(\mathbf{q}_M)$ at the midpoint and identify the set $\mathcal{I} = \{i \,|\, g_{Ni}(\mathbf{q}) \leqslant 0\}$ of closed contacts. Calculate the contact velocities $\gamma_{A*_i} = \mathbf{w}_{*M_i}^{\mathrm{T}}\mathbf{u}_A \quad \forall i \in \mathcal{I}$ at the beginning of the time step, where $*$ has been used generically for N, T, τ and R.

4) Solve the contact problem using the fixed-point iteration scheme:

$$\mathbf{u}_E^k = \mathbf{u}_A + \mathbf{M}_M^{-1}\left(\mathbf{h}_M\Delta t + \mathbf{W}_{NM}P_{Ni}^k + \mathbf{W}_{TM}\mathbf{P}_{Ti}^k + \mathbf{W}_{\tau M}P_{\tau i}^k + \mathbf{W}_{RM}P_{Ri}^k\right) \tag{4.1}$$

$$\gamma_{E*_i} = \mathbf{w}_{*M_i}^{\mathrm{T}}\mathbf{u}_E^k \qquad \forall i \in \mathcal{I} \tag{4.2}$$

$$\xi_{*_i} = \gamma_{E*_i} + e_i\gamma_{A*_i} \qquad \forall i \in \mathcal{I} \tag{4.3}$$

$$P_{Ni}^{k+1} = -\mathrm{prox}_{C_{N_i}}\left(-P_{Ni}^k + r_N\,\xi_{N_i}^k\right) \qquad \forall i \in \mathcal{I} \tag{4.4}$$

$$\mathbf{P}_{Ti}^{k+1} = -\mathrm{prox}_{C_{T_i}(C_{N_i})}\left(-\boldsymbol{P}_{Ti}^k + r_T\,\boldsymbol{\xi}_{T_i}^k\right) \qquad \forall i \in \mathcal{I} \tag{4.5}$$

$$P_{\tau i}^{k+1} = -\mathrm{prox}_{C_{\tau_i}(C_{N_i})}\left(-P_{\tau i}^k + r_\tau\,\xi_{\tau_i}^k\right) \qquad \forall i \in \mathcal{I} \tag{4.6}$$

$$P_{Ri}^{k+1} = -\mathrm{prox}_{C_{R_i}(C_{N_i})}\left(-P_{Ri}^k + r_R\,\xi_{R_i}^k\right) \qquad \forall i \in \mathcal{I} \tag{4.7}$$

As stopping criterion, we use the summed force difference

$$error = \sum_{i\in\mathcal{I}}\left(|P_{Ni}^{k+1} - P_{Ni}^k| + \|\mathbf{P}_{Ti}^k - \mathbf{P}_{Ti}^k\|_2 + |P_{\tau i}^{k+1} - P_{\tau i}^k| + |P_{Ri}^{k+1} - P_{Ri}^k|\right) < \text{tol.}$$

5) Upon convergence of the iteration in 4) giving $\mathbf{u}_E$, the position $\mathbf{q}_E$ at t_E is updated as $\mathbf{q}_E = \mathbf{q}_M + \frac{1}{2}\mathbf{F}(\mathbf{q}_M)\mathbf{u}_E\,\Delta t$.

In the above scheme we see how various contact force laws have been taken into account. At this point we have to mention that the scheme above is only valid for separated Coulomb and pivoting friction. For other friction models, like Coulomb – Contensou friction or smoothed Coulomb friction, we have to modify this scheme by replacing the corresponding contact laws.

4.1. Simulation of the Model with Bilateral Constraint

For a spinning disk in persistent contact with the support we may formulate the dynamics as an ODE and solve it with standard methods for ordinary differential equations. Under the hypothesis that the contact point C_1 does not detach during the inversion, we formulate a bilateral constraint $g_{N1}(\mathbf{q}) = 0$, such that the contact point C_1 remains always in contact with the ground. If this constraint is initially satisfied on position level $g_{N1}(\mathbf{q}_0) = 0$, we obtain the constraint equation on velocity level as

$$\gamma_{N1}(\mathbf{q}, \mathbf{u}) = \mathbf{w}_{N1}^{\mathrm{T}}\, \mathbf{u} = 0. \tag{4.8}$$

Through derivation of the constraint on velocity level (4.8) with respect to time, we obtain for $g_{N1}(\mathbf{q}_0) = \gamma_{N1}(\mathbf{q}_0, \mathbf{u}_0) = 0$ the bilateral constraint equation

$$\begin{aligned} \dot{\gamma}_{N1}(\mathbf{q}, \mathbf{u}, \dot{\mathbf{u}}) &= \frac{\partial \gamma_{N1}(\mathbf{q}, \mathbf{u})}{\partial \mathbf{u}}\, \dot{\mathbf{u}} + \dot{\mathbf{w}}_{N1}^{\mathrm{T}} \mathbf{u} \\ &= \mathbf{w}_{N1}^{\mathrm{T}}\, \dot{\mathbf{u}} + \dot{\mathbf{w}}_{N1}^{\mathrm{T}} \mathbf{u} = 0, \end{aligned} \tag{4.9}$$

on acceleration level. Equation (4.9) forms under the assumption of only pure Coulomb friction (i. e., no additional friction forces like contour or pivoting friction) together with the kinematic equation and the equation of motion from (3.39) or (3.67) a linear system of equations

$$\underbrace{\begin{bmatrix} \mathbf{I} & \mathbf{0} & \mathbf{0} \\ \mathbf{0} & \mathbf{M} & -\mathbf{W}_{NT} \\ \mathbf{0} & \mathbf{w}_{N1}^{\mathrm{T}} & \mathbf{0} \end{bmatrix}}_{\mathbf{A}} \begin{bmatrix} \dot{\mathbf{q}} \\ \dot{\mathbf{u}} \\ \lambda_N \end{bmatrix} = \begin{bmatrix} \mathbf{F}(\mathbf{q})\, \mathbf{u} \\ \mathbf{h} + \mathbf{f}_g \\ -\dot{\mathbf{w}}_{N1}^{\mathrm{T}}\, \mathbf{u} \end{bmatrix}. \tag{4.10}$$

As the tangential force is linear in λ_N, we define $\mathbf{W}_{NT} := \mathbf{w}_{N1} - \mu \mathbf{W}_{T1} \frac{\gamma_{T1}}{\|\gamma_{T1}\| + \varepsilon}$ as the generalized force direction describing both normal and tangential force. The matrix $\mathbf{A}$ is of full rank, such that the system (4.10) can be integrated with every standard integrator for ordinary differential equations (e.g., the stiff integrator *ode*15*s* from MATLAB).

5. DIMENSIONS

We consider a stainless steel disk with the following dimensions and mass properties. The simplest way to fabricate a disk where the geometric center G and the center of gravity S do not coincide is to take a homogeneous disk and to drill a hole with radius a at a defined distance L with respect to G, see Fig. 5.

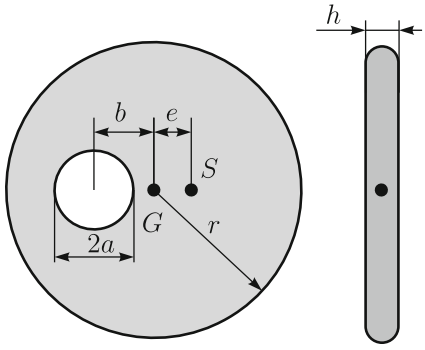

Fig. 5. Dimensions of the tippedisk.

The eccentricity e then follows as $e = \frac{ba^2}{(r^2 - a^2)}$. Since we assume an infinitely thin disk, we will also neglect the rounding to calculate the mass properties and refrain from introducing a parameter describing the rounding of the disk. In Table 1, the dimensions of the tippedisk are listed.

Table 1. Dimensions of the tippedisk.

Property	Parameter	Magnitude	Unit
Disk radius	r	0.045	m
Hole radius	a	0.015	m
Distance	b	0.02	m
Disk height	h	0.01	m
Eccentricity	e	$2.5 \cdot 10^{-3}$	m

The inertia tensor of the homogeneous disk, with mass m_h, radius r and height h is given in the principal axis system, with respect to the geometric center, as

$$ {}_B\mathbf{\Theta}_{\mathrm{hom},G} = \begin{bmatrix} \frac{1}{12}\, m_h(h^2 + 3\, r^2) & 0 & 0 \\ 0 & \frac{1}{12}\, m_h(h^2 + 3\, r^2) & 0 \\ 0 & 0 & \frac{6}{12}\, m_h r^2 \end{bmatrix}, \tag{5.1} $$

with mass $m_h = \rho\pi r^2 h$. For the homogeneous disk, the center of gravity S and the geometric center G coincide. Since we aim to calculate the inertia tensor of the tippedisk with respect to the geometric center G, we have to subtract the hole under consideration of the parallel axis theorem. We introduce the reduced mass m_r with a negative magnitude $m_r = -\rho\pi a^2 h$ and we obtain the inertia tensor of the hole, with respect to G, as

$$ {}_B\mathbf{\Theta}_{\mathrm{h},G} = \begin{bmatrix} \frac{1}{12}\, m_r(h^2 + 3\, a^2) & 0 & 0 \\ 0 & \frac{1}{12}\, m_r(h^2 + 3\, a^2) + m_r b^2 & 0 \\ 0 & 0 & \frac{6}{12}\, m_r a^2 + m_r b^2 \end{bmatrix}. \tag{5.2} $$

The inertia tensor of the tippedisk then follows as ${}_B\mathbf{\Theta}_G = {}_B\mathbf{\Theta}_{\mathrm{hom},G} + {}_B\mathbf{\Theta}_{\mathrm{h},G}$. The respective magnitudes of the principal moment of inertia are listed in Table 2.

Table 2. Inertia properties of the tippedisk.

Property	Formula	Magnitude	Unit
Density ρ	—	7700	kg/m^3
Mass m	$m_h + m_r = \rho\,\pi(r^2 - a^2)\,h$	0.435	kg
${}_B\mathbf{\Theta}_G(1,1) = A$	$\frac{\rho\pi h}{12}\left(3r^4 + r^2h^2 - a^2h^2 - 3a^4\right)$	$0.249 \cdot 10^{-3}$	kg m^2
${}_B\mathbf{\Theta}_G(2,2) = B$	$\frac{\rho\pi h}{12}\left(3r^4 + r^2h^2 - a^2h^2 - 3a^4 - 12a^2b^2\right)$	$0.227 \cdot 10^{-3}$	kg m^2
${}_B\mathbf{\Theta}_G(3,3) = C$	$\frac{\rho\pi h}{12}\left(6r^4 - 6a^4 - 12a^2b^2\right)$	$0.468 \cdot 10^{-3}$	kg m^2

6. SIMULATION RESULTS

In this section, the simulation results for various models are presented and discussed. As shown in Fig. 6, we call the tippedisk *not inverted* if $\beta = \frac{\pi}{2}$ and $\gamma = -\frac{\pi}{2}$ holds, such that the center of gravity S lies below the geometric center G. Vice versa, we call the disk *inverted* if $\beta = \frac{\pi}{2}$ and $\gamma = \frac{\pi}{2}$ holds. Note that this definition is not unique, as $\beta = -\frac{\pi}{2}$ and $\gamma = \frac{\pi}{2}$ describes also an inverted orientation of the tippedisk. Since we can restrict the inclination angle to $\beta \in [0, \pi)$ in the following, this ambiguity is not present.

The initial conditions, at time $t_0 = 0$s, for all reported simulations are given in Table 3. The simulation end time was set to $t_1 = 5$s, with time step $\Delta t = 10^{-5}$s. The initial conditions were

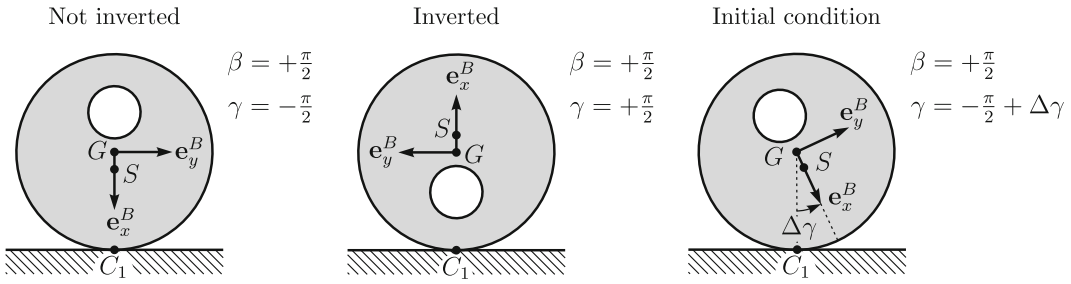

Fig. 6. Stationary solutions of the tippedisk.

chosen such that the disk spins in a perturbed noninverted orientation ($\Delta\gamma = 0.1\,\text{rad}$), without slip and in persistent contact with the support, see Fig. 6. The corresponding coordinates and velocities for the quaternion-based approaches can be calculated from the rotation matrix

$$\mathbf{R} = \mathbf{R}(\boldsymbol{\varphi}) = \mathbf{R}(\mathbf{p}), \tag{6.1}$$

and the kinematic coupling

$$\begin{bmatrix} \dot{x}_0 \\ \dot{y}_0 \\ \dot{z}_0 \\ \omega_{x0} \\ \omega_{y0} \\ \omega_{z0} \end{bmatrix} = \begin{bmatrix} \mathbf{I} & \mathbf{0} \\ \mathbf{0} & {}_B\mathbf{J}_R \end{bmatrix} \begin{bmatrix} \dot{x}_0 \\ \dot{y}_0 \\ \dot{z}_0 \\ \dot{\alpha}_0 \\ \dot{\beta}_0 \\ \dot{\gamma}_0 \end{bmatrix}, \tag{6.2}$$

where ${}_B\mathbf{J}_R$ is given by (3.6). The initial condition for the quaternion-based model can be calculated from Table 3. The friction and restitution coefficients are given as

Friction properties: $\mu_T = 0.3, \mu_\tau = \frac{\mu_T}{100}, \mu_R = \frac{\mu_T}{100}, \varepsilon = 0.1$

Restitution coefficients: $e_N = e_T = e_\tau = e_R = 0$

The time-stepping tolerance was set to $tol = 10^{-8}$. Furthermore, in the proximal point iteration we choose $r_N = r_T = r_\tau = 0.1$ and $r_R = 10^{-4}$. In the following, we will discuss several simulation settings with the same initial conditions, but different rotation parameters and modeling levels, listed in Table 4. The abbreviation "E" denotes a model with Euler angles and "Q" stands for a quaternion-based model.

Table 3. Initial conditions.

Coordinate	Magnitude	Unit	Velocity	Magnitude	Unit
x_0	0	m	$\dot{x}_0$	0	m/s
y_0	0	m	$\dot{y}_0$	0	m/s
z_0	0.045	m	$\dot{z}_0$	0	m/s
α_0	0	rad	$\dot{\alpha}_0$	40	rad/s
β_0	0.5π	rad	$\dot{\beta}_0$	0	rad/s
γ_0	$-0.5\pi + 0.1$	rad	$\dot{\gamma}_0$	$-\dot{\alpha}_0 \cos(\beta_0) = 0$	rad/s

Table 4. Various models with different parametrizations and force laws.

Model	—	Integrator	Dissipation Mechanisms
ODE Model 1	E	*ode*15*s*	smooth Coulomb
ODE Model 2	Q	*ode*15*s*	smooth Coulomb
Model 1	E	Moreau	set-valued Coulomb
Model 2	Q	Moreau	set-valued Coulomb
Model 3	E	Moreau	Coulomb – Contensou
Model 4	Q	Moreau	Coulomb – Contensou
Model 5	E	Moreau	smooth Coulomb
Model 6	Q	Moreau	smooth Coulomb
Model 7	E	Moreau	set-valued Coulomb, pivoting, contour
Model 8	Q	Moreau	set-valued Coulomb, pivoting, contour
Model 9	E	Moreau	smooth Coulomb, pivoting, contour
Model 10	Q	Moreau	smooth Coulomb, pivoting, contour

6.1. Time-stepping with Set-valued Coulomb Friction

In Fig. 7, the results obtained for the models with set-valued Coulomb friction (Model 1 and Model 2) are depicted. The upper left graph shows the time evolution of the Euler angles β (blue, dotted) and γ (red, dashed). For $t = 0$, the tippedisk is near to the noninverted solution. After a short time, the angle γ increases and a periodic oscillation around the inverted configuration occurs. During this process, the angle β does only change slightly, whereas the angle γ is oscillating with a large amplitude. The height z_S of the center of gravity S increases during the inversion process, but instead of reaching the fully inverted height $r + e$, it oscillates aperiodically around 0.044 (arithmetic mean of z_S for $t \in [1s, 5s]$, for the model in Euler angles). The energy plots in

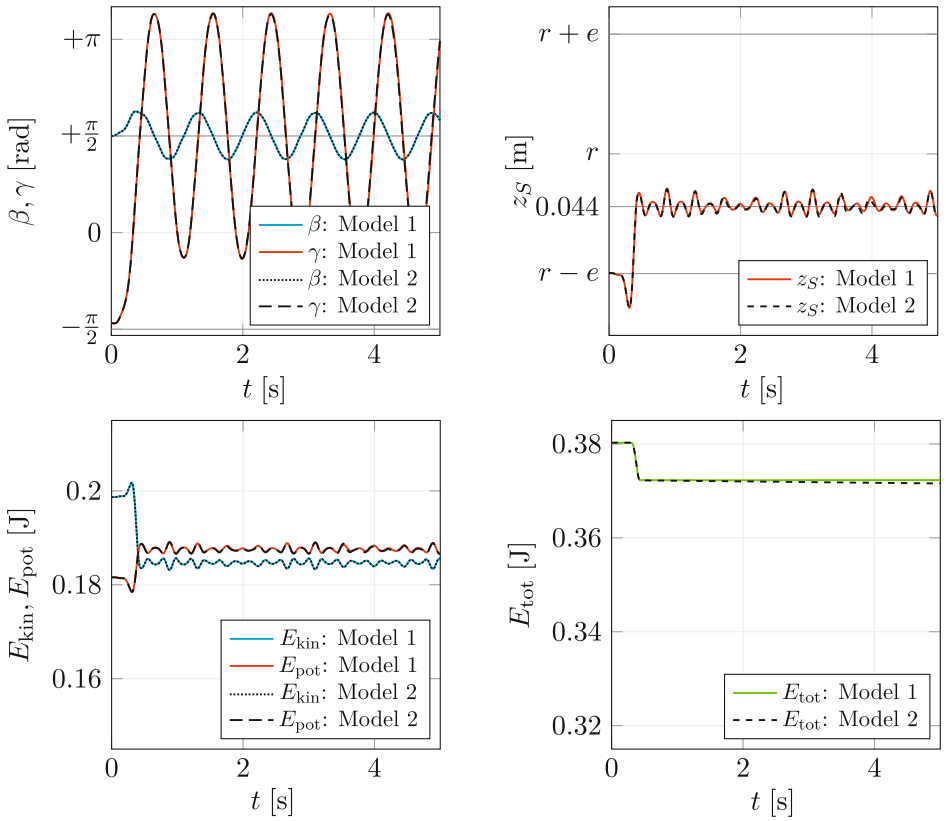

Fig. 7. Simulation results for set-valued Coulomb friction.

the second row show that the potential energy E_{pot} (red, dashed) increased and the kinetic energy E_{kin} (blue, dotted) decreased during the transient dynamics $t \in [0s, 0.5s]$. The total energy E_{tot} reveals energy dissipation during $t \in [0s, 0.5s]$ and remains almost constant after $0.5s$. The kinetic and potential energy are exchanged complementarily.

Figure 8 shows that the contact distance g_{N1} of the contact point C_1 is always nonpositive but nearly zero, such that the contact point C_1 does not detach. For the Model 1 in Euler angles, the contact distance g_{N1} changes with high frequency between 0 and $-2 \cdot 10^{-9}$ m. Using the quaternion-based Model 2, the height of the contact point C_1 decreases monotonically, i.e., the simulation suffers from constraint drift, as no correction has been applied at the end of each time step.

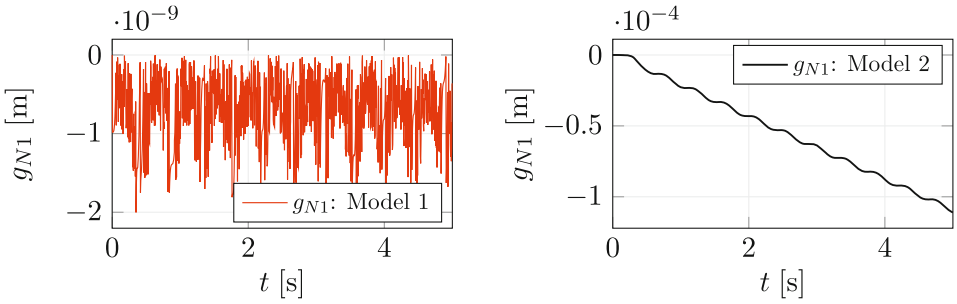

Fig. 8. Contact distance g_{N1} for set-valued Coulomb friction.

6.2. Time Stepping with Coulomb – Contensou Friction

Figure 9 shows the simulation results for Model 3 with Euler angles and the quaternion-based Model 4 under consideration of Coulomb – Contensou friction. Contour friction is neglected. According to the γ-graph (red, dashed), we observe an inversion on the interval $t \in [0s, 0.5s]$, i. e., that the angle γ rises to $\gamma = \frac{\pi}{2}$. After the rise, a damped oscillation occurs, such that the inverted

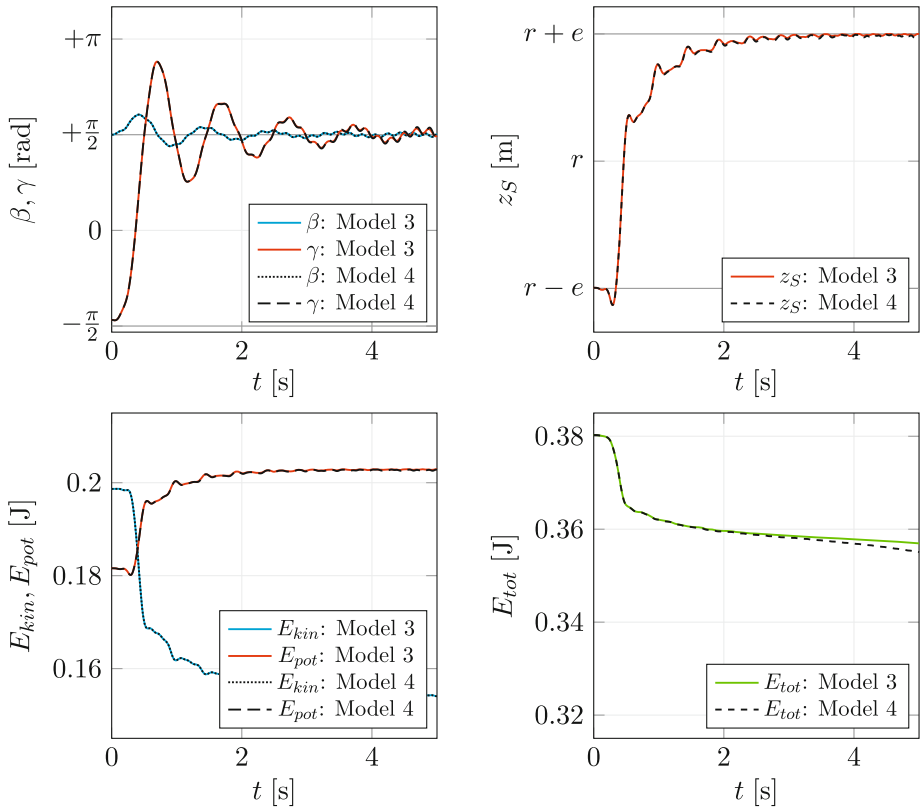

Fig. 9. Simulation results for Coulomb – Contensou friction.

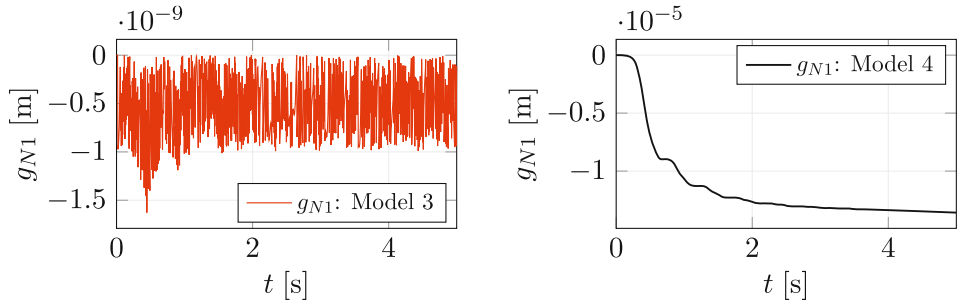

Fig. 10. Contact distance g_{N1} for Coulomb – Contensou friction.

orientation $\gamma = \frac{\pi}{2}$ seems to be asymptotically stable. The inclination angle β (blue, dotted) performs a damped oscillation around $\beta = \frac{\pi}{2}$. In both graphs γ and β start to oscillate with high frequency at $t \approx 2s$. The height of the center of gravity drops slightly before growing to the inverted height $r + e$. The lower graphs of Fig. 9 depict the energy. Here we observe that the potential energy E_{pot} (red, dashed) increases, whereas the kinetic energy E_{kin} (blue, dotted) decreases during the inversion. As Coulomb – Contensou friction dissipates, the total energy E_{tot} (green, dashed) decreases fast during the inversion process. After the inversion, the rate of dissipation drops, but remains unequal to zero.

The contact distance g_{N1} of the contact point C_1 behaves similarly to the results based on set-valued Coulomb friction. As in Model 2, the simulation suffers from constraint drift, which saturates at $-1.36 \cdot 10^{-5}$ m.

6.3. Time Stepping with Smooth Coulomb Friction

Figure 11 shows simulation results for Model 5 with Euler angles and the quaternion-based Model 6 under consideration of smooth Coulomb friction. Contour and pivoting friction are

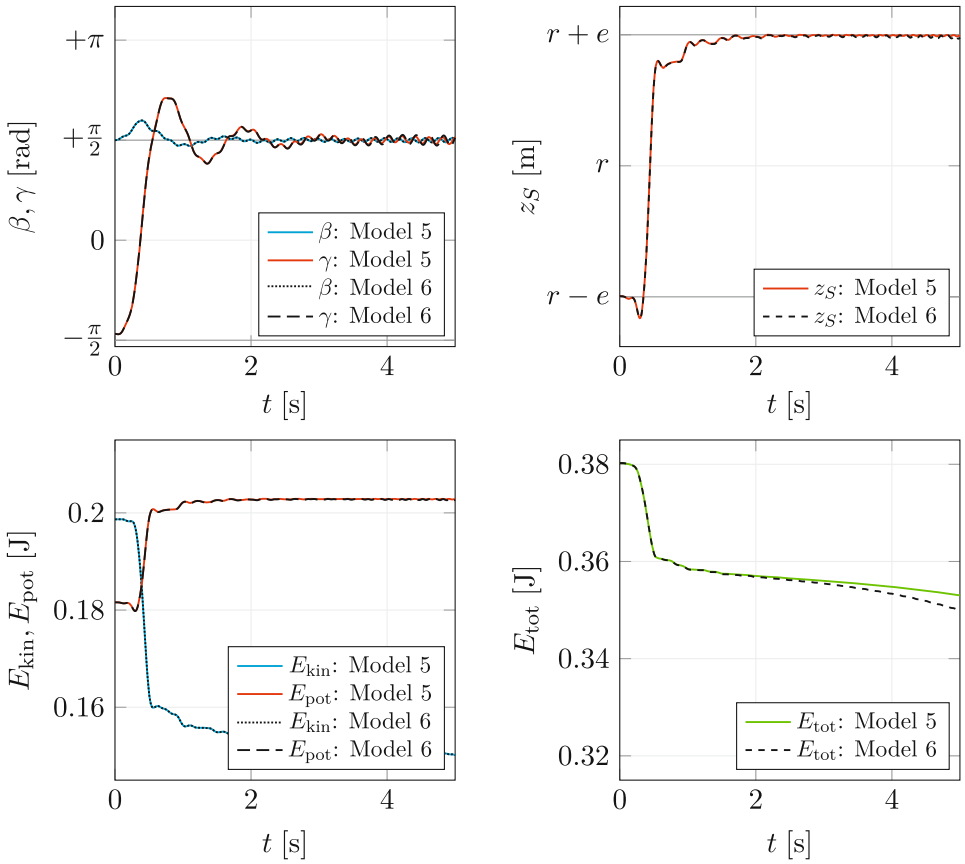

Fig. 11. Simulation results for smooth Coulomb friction.

neglected. According to the γ-graph (blue, dotted), the disk tends to invert directly on the interval $t \in [0s, 0.5s]$. After the inversion, a damped oscillation around $\gamma = \frac{\pi}{2}$ occurs, such that the inverted solution seems to be asymptotically stable. The inclination angle β (red, dashed) undergoes damped oscillations around $\beta = \frac{\pi}{2}$. In both graphs γ and β small oscillations with high frequency start to occur at $t \approx 1s$. In the upper right graph, the height of the center of gravity drops slightly and then grows asymptotically to the inverted height $r + e$ of the center of gravity S. In the second row of Fig. 11 the energy graphs show that the kinetic energy E_{kin} (blue, dotted) decreases during the inversion process, whereas the potential energy E_{pot} (red, dashed) increases. The total energy E_{tot} (green, dashed) decreases fast during the inversion. After the inversion, the total energy tends to decrease slowly.

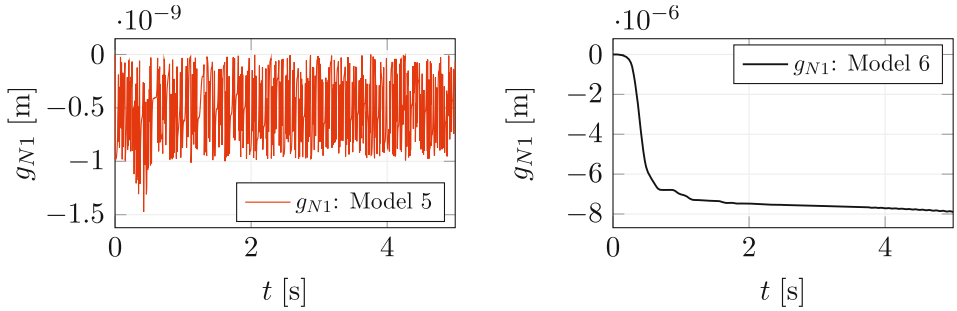

Fig. 12. Contact distance g_{N1} for smooth Coulomb friction.

As in the case of set-valued Coulomb friction, we observe the contact distance g_{N1} not to get greater than zero for the case of smooth Coulomb friction, Fig. 12. The parameterization in Euler angles leads to an aperiodic oscillation of the height of C_1, in a band with width of 10^{-9} m. The gap distance g_{N1} for the quaternion-based model decreases, starting at 0 m and saturating at $-7.5 \cdot 10^{-6}$ m.

6.4. Ordinary Differential Equation with Smooth Coulomb Friction

The results of the simulations with smooth Coulomb friction, neglecting other dissipative forces, are presented in Fig. 13. After $t = 0$ s the angle γ rises quickly from $-\frac{\pi}{2}$ and results in an asymptotic oscillation around $+\frac{\pi}{2}$. During this process the inclination angle β does only change slightly.

Both responses of the angles β and γ are increasingly superimposed by small oscillations with higher frequency. The height of the center of gravity S is shown in the z_S-graph and is growing from $r - e$ to $r + e$ and therefore the disk starts in the noninverted configuration and ends in an inverted solution. In the process of inversion the total energy dissipates from 0.28 J to 0.36 J. After this fast dissipation $t < 0.5$ s the total energy slowly decreases. In contrast to the previous models with unilateral contact, we do not have to consider the height of the contact point C_1, since we introduced a bilateral constraint on the gap g_{N1}.

6.5. Comparison

Figure 14 compares the introduced models using different force laws and therefore different dissipation mechanisms. As Euler angle and quaternion-based models lead to almost the same results, we only discuss solutions obtained by the quaternion-based approach to keep the following plots clearer. The left graph depicts the evolution of the angle γ. For set-valued Coulomb friction, Model 2 (red), the solution settles on a periodic oscillation around $\gamma = \frac{\pi}{2}$ with slightly increasing amplitude. If contour and pivoting friction is added, see Model 8 (black, $*$), we obtain similar behavior to pure set-valued Coulomb friction during the transient process. After the transient dynamics, more energy is dissipated during the periodic oscillation, such that the amplitude increases significantly.

The γ-graph under the assumption of set-valued Coulomb – Contensou friction (Model 4) shows that γ increases during the inversion process. After the transient interval $t \in [0, 0.3\,\text{s}]$, a decaying

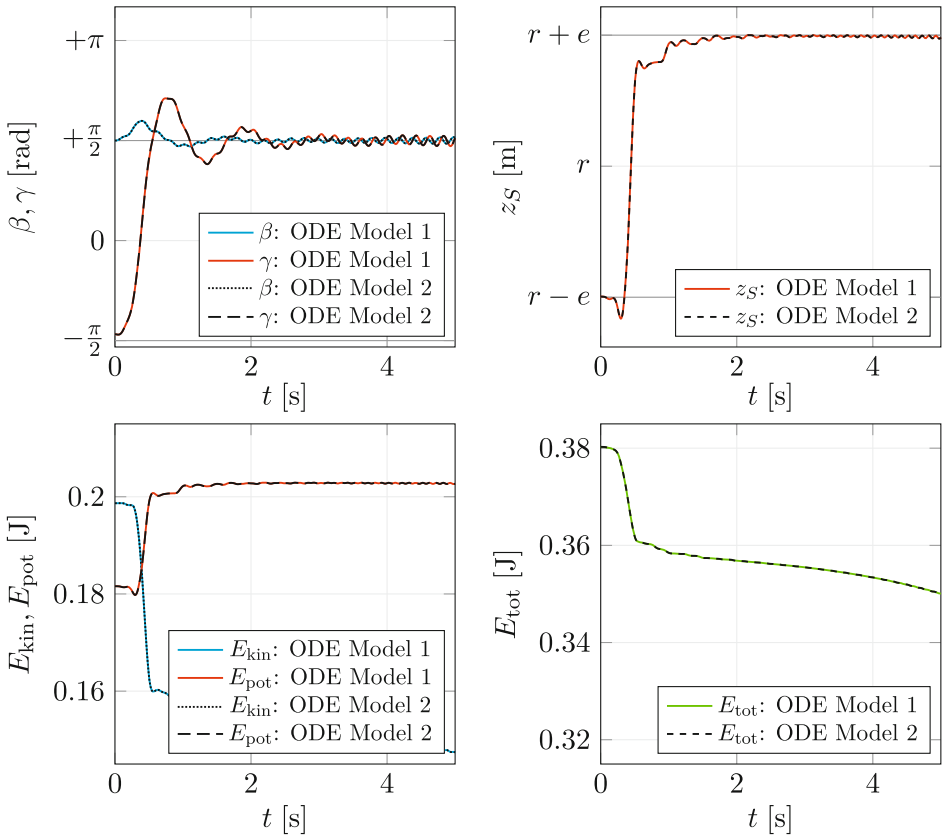

Fig. 13. Simulation results for smooth Coulomb friction using an ODE.

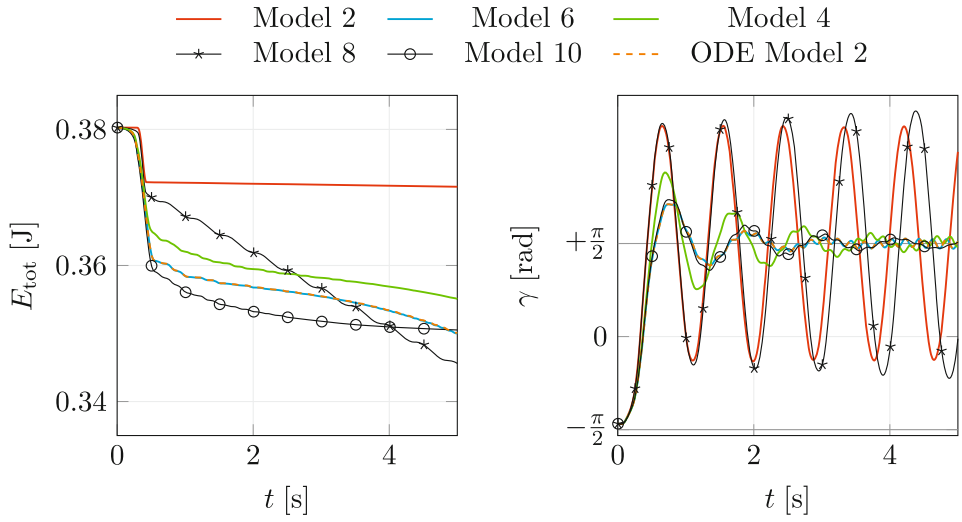

Fig. 14. Comparison of the introduced models.

oscillation occurs, such that the disk ends in an inverted configuration. Smooth Coulomb friction, Model 6 (blue), leads to qualitatively similar behavior as Coulomb – Contensou friction. The evolution of the angle γ for smooth Coulomb friction with contour and separated pivoting friction (Model 10) is depicted in (black, o). The additional dissipation mechanisms affect the inversion slightly. The solution for the ODE Model 2 (orange, dashed) is almost identical to the solution of Model 6, i.e., the difference in the γ-angle between Model 6 and ODE Model 2 fluctuates approximately between $+10^{-3}$ rad and -10^{-3} rad. The right plot of Fig. 14 shows the total

energy E_{tot} for the specified models. We observe that pivoting and contour friction are leading to more dissipation. However, these additional dissipation mechanisms do not have a significant effect on the inversion phenomenon. It is striking that the solutions of the models with more advanced dissipation mechanisms do not differ qualitatively from the model with pure spatial friction for short time scales, which can be explained through the fact that the inverted orientation is reached in a shorter time and, therefore, with less dissipation. For the long-term behavior, however, these additional dissipation mechanisms play an important role. In Fig. 15, the angle γ is depicted for the time interval $t \in [0, 25\text{s}]$. The green graph describes the γ-solution using the quaternion-based Model 4 with Coulomb – Contensou friction, neglecting additional frictional effects. After the inversion, an increasing vibration around $+\frac{\pi}{2}$ occurs, until the tippedisk falls down at $t \approx 17\text{s}$. Both models with pure, smooth Coulomb friction, Model 6 and ODE Model 2, are leading to similar behavior. After γ converges to $+\frac{\pi}{2}$, energy is being dissipated, such that the disk falls down and comes to rest. This decay depends strongly on the chosen friction parameters.

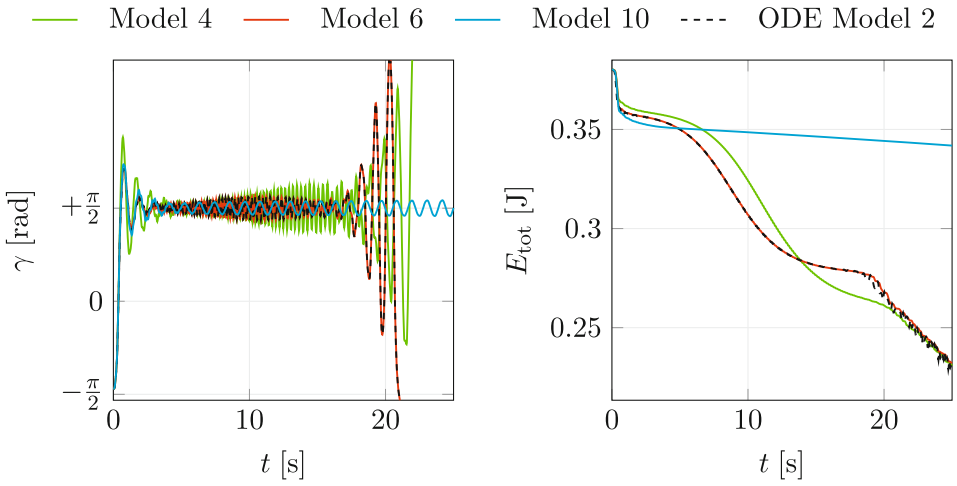

Fig. 15. Long-term behavior.

The evolution of γ for Model 10, i.e, under smooth Coulomb, contour and pivoting friction is shown in the blue graph. As γ increases, the solution oscillates and converges to $+\frac{\pi}{2}$. After $t \approx 5\text{s}$ this decaying solution seems to end in a periodic oscillation with constant amplitude. As there will be always dissipation, this oscillation cannot be a limit set for this system, such that the disk will also end in the horizontal configuration. At this point we mention that the different long-term behavior depends on the applied dissipation mechanisms and cannot be attributed to convergence problems, as we checked the solution using the models with quaternions and Euler angles. In the right-hand plot the total energy E_{tot} is depicted for the long-term simulation. Here it is counterintuitive that Model 10 stays for a longer time in the inverted configuration, although more dissipation effects were considered. In summary, it can be stated that the dissipation mechanisms hardly play a role during the inversion process. However, the long-term behavior of the tippedisk heavily depends on the applied friction laws. In Fig. 16, the inversion of the tippedisk is shown as an image sequence that comes from recordings with a high-speed camera at 500 fps. The initial angular velocity, in the noninverted configuration, was $\dot{\alpha} \approx -50\,[\text{rad/s}]$. To compare this experiment with the numerical experiment using Euler angles and smooth Coulomb friction (ODE Model 1), a second image sequence is shown in Fig. 17, with initial angular velocity $\dot{\alpha} = -50\,[\text{rad/s}]$. The visual comparison between both stroboscopic image sequences shows that the presented model is sufficiently accurate to describe the real system qualitatively during the inversion process. Here we point out that the numerical model used in Fig. 17 has not been fitted to the experiment. Nevertheless, we achieve astonishing agreement between the numerical and the laboratory experiment.

7. DISCUSSION

The comparison of the introduced models shows that set-valued Coulomb friction is not sufficient to describe the inversion phenomenon, as γ keeps oscillating periodically in Fig. 14. More specifically,

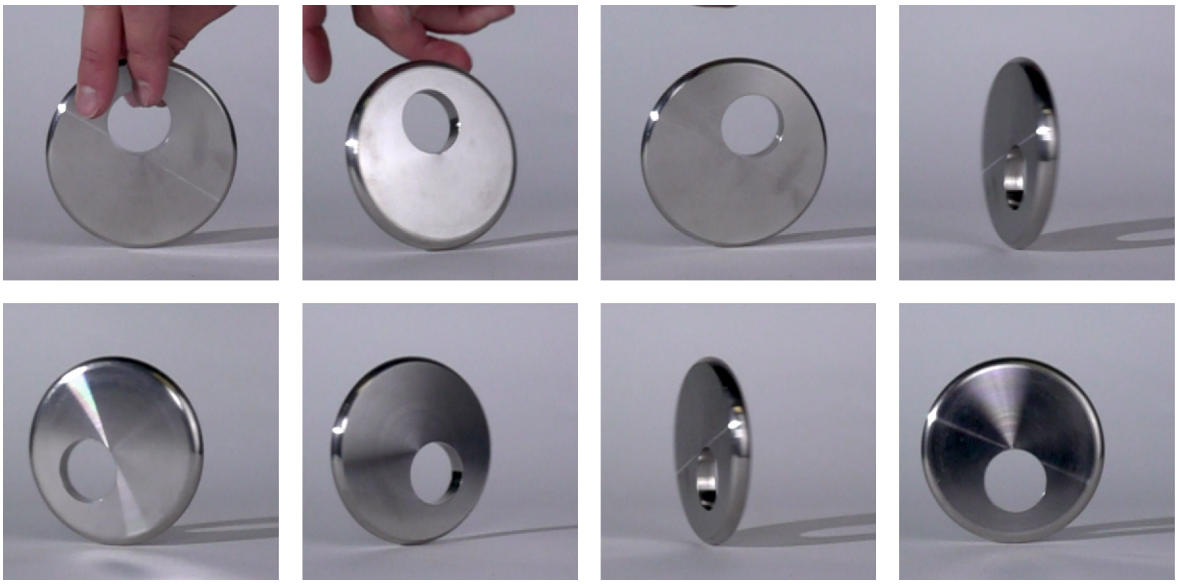

Fig. 16. Experiment: stroboscopic images of the inversion

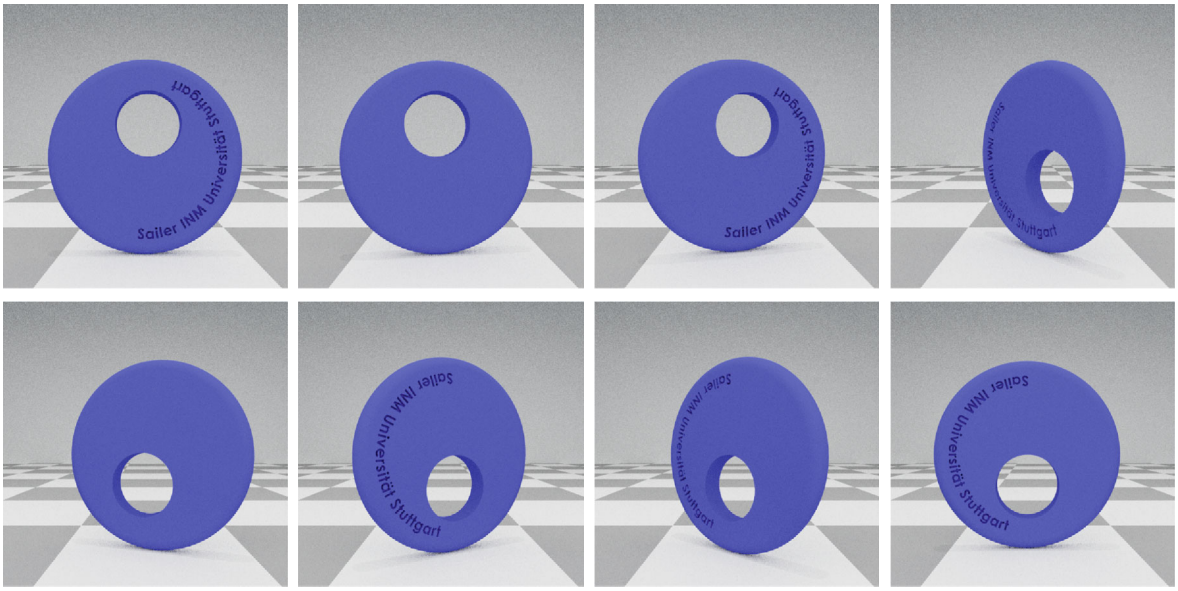

Fig. 17. Numerical experiment: stroboscopic images of the inversion.

in the case of set-valued Coulomb friction, the tippedisk ends in a state of pure rolling, for which the center of gravity S does not lie above the geometric center G of the disk. The smoothing of the set-valued force law, which is motivated through Coulomb – Contensou friction [17] characterizes the inversion phenomenon and leads to results which agree with experiments (Figs. 16 and 17). Furthermore, it has been shown by the time-stepping simulations that the contact point C_1 does not detach from the flat support during the process of inversion. This supports the assumption of the bilateral constraint, introduced in Eq. (4.8). In Fig. 14, the evolution of the angle γ is depicted in the left graph for the most important models. Comparing the angle γ of the time-stepping model with smooth Coulomb friction with the smooth ODE-models, it follows that both solutions are similar with respect to numerical error. In the case of smooth Coulomb friction, pivoting friction and contour friction we observe a similar qualitative inversion behavior as in the case of (only) smooth Coulomb friction. It is striking that the solutions of the models with more advanced dissipation mechanisms do not differ from the model with pure Coulomb friction for

short time scales. For long-term behavior the effects of additional dissipation cannot be neglected. For $\varepsilon \downarrow 0$, the solutions under smooth Coulomb friction converge to the solutions under set-valued Coulomb friction. If the smoothing parameter ε is set to zero, the smooth force laws are not defined for zero slip, i. e., $\boldsymbol{\gamma}_T = 0$. Furthermore, the correctness and convergence of the individual solutions are checked by agreement between the quaternion-based models and the models in Euler angles. Numerical experiments revealed that all quaternion-based models converge faster for decreasing time steps. In contrast, the models in Euler angles do not suffer from constraint drift as much as the quaternion-based models. This penetration in the time-stepping solutions is a relic from Signorini's law on velocity level used to formulate set-valued force laws which combine Signorini's normal and Newton's impact law in one force law. To prevent these inadmissible penetrations, it is convenient to correct the generalized coordinates after each time step. Since these penetrations are negligible for the inversion phenomenon presented here, we will not discuss constraint violation in this paper. However, we have to mention that simple constraint violation can lead to an increasing penetration of the contact point C_1. To prevent these induced drifts, more advanced projection techniques exist, see [15]. The results obtained are sufficiently exact without any corrections, and the presented models with regularized Coulomb friction are able to describe the inversion phenomenon.

8. CONLUSIONS

In this work the tippedisk has been introduced as a new scientific toy to the playground of mechanical mathematical archetypes for gyroscopic systems under unilateral constraints and friction. We modeled the tippedisk on different modeling levels and compared quaternion-based models with models in Euler angels. To describe the inversion phenomenon, regularized Coulomb friction is sufficient and motivated by the set-valued Coulomb – Contensou friction. The models in Euler angles and the quaternion-based models have each their own advantages. The quaternion-based models converge faster, but lead to more pronounced inadmissible penetration of the contact point if no constraint correction is applied. The long-term behavior of the disk depends strongly on the chosen dissipation mechanisms. Therefore, we have to take other force laws, such as Coulomb – Contensou friction, pivoting and contour friction into account as these dissipation mechanisms specify the long-term behavior. Hence, the time and the trajectory from inverted spinning to the state of rest depend strongly on these advanced friction laws. Since we are interested in the short-term inversion phenomenon, we will use the minimal model in Euler angles with regularized Coulomb friction to describe the dynamics of the tippedisk qualitatively using techniques from nonlinear dynamics in future research. Moreover, the numerical model serves as reference to validate the results of later experiments. This paper also reports preliminary experimental results and shows the qualitative correspondence with numerical simulations. More extensive experimental analysis is needed to validate the friction models and needs to be compared quantitatively with numerical simulations. In summary, it should be noted that the tippedisk cannot be understood as a trivial generalization of the tippetop, since the dynamics is different and therefore much more complex, such that we cannot describe the inversion phenomenon using intuitive considerations. In addition, the tippedisk serves as a link between analytical, theoretical mechanics and nonlinear dynamics, and the models obtained in this work provide the basis for further research on the dynamics of the tippedisk.

CONFLICT OF INTEREST

The authors declare that they have no conflicts of interest.

REFERENCES

1. Acary, V. and Brogliato, B., *Numerical Methods for Nonsmooth Dynamical Systems: Applications in Mechanics and Electronics,* Lect. Notes Appl. Comput. Mech., vol. 35, Berlin: Springer, 2008.
2. Ashbaugh, M. S., Chicone, C. C., and Cushman, R. H., The Twisting Tennis Racket, *J. Dynam. Differential Equations,* 1991, vol. 3, no. 1, pp. 67–85.
3. Borisov, A. V., Kilin, A. A., and Karavaev, Yu. L., On the Retrograde Motion of a Rolling Disk, *Physics-Uspekhi,* 2017, vol. 60, no. 9, pp. 931–934; see also: *Uspekhi Fiz. Nauk,* 2017, vol. 187, no. 9, pp. 1003–1006.
4. Borisov, A. V. and Mamaev, I. S., Strange Attractors in Rattleback Dynamics, *Physics-Uspekhi,* 2003, vol. 46, no. 4, pp. 393–403; see also: *Uspekhi Fiz. Nauk,* 2003, vol. 173, no. 4, pp. 407–418.
5. Borisov, A. V., Mamaev, I. S., and Kilin, A. A., Dynamics of Rolling Disk, *Regul. Chaotic Dyn.,* 2003, vol. 8, no. 2, pp. 201–212.

6. Bou-Rabee, N. M., Marsden, J. E., and Romero, L. A., Tippe Top Inversion As a Dissipation-Induced Instability, *SIAM J. Appl. Dyn. Syst.,* 2004, vol. 3, no. 3, pp. 352–377.
7. Cohen, C. M., The Tippe Top Revisited, *Am. J. Phys.,* 1977, vol. 45, no. 1, pp. 12–17.
8. Garcia, A. and Hubbard, M., Spin Reversal of the Rattleback: Theory and Experiment, *Proc. Roy. Soc. London Ser. A,* 1988, vol. 418, no. 1854, pp. 165–197.
9. Glocker, Ch., *Set-Valued Force Laws: Dynamics of Non-smooth Systems,* Lect. Notes Appl. Comput. Mech., vol. 1, Berlin: Springer, 2013.
10. Glocker, Ch., Simulation of Hard Contacts with Friction: An Iterative Projection Method, in *Recent Trends in Dynamical Systems,* A. Johann, H.-P. Kruse, F. Rupp, S. Schmitz (Eds.), Springer Proc. Math. Stat., vol. 35, Basel: Springer, 2013, pp. 493–515.
11. Hemingway, E. G. and O'Reilly, O. M., Perspectives on Euler Angle Singularities, Gimbal Lock, and the Orthogonality of Applied Forces and Applied Moments, *Multibody Syst. Dyn.,* 2018, vol. 44, no. 1, pp. 31–56.
12. Jachnik, J., Spinning and Rolling of an Unbalanced Disk, *Master's Thesis,* London: Imperial College London, 2011.
13. Karapetyan, A. V. and Zobova, A. A., Tippe-Top on Visco-Elastic Plane: Steady-State Motions, Generalized Smale Diagrams and Overturns, *Lobachevskii J. Math.,* 2017, vol. 38, no. 6, pp. 1007–1013.
14. Kessler, P. and O'Reilly, O. M., The Ringing of Euler's Disk, *Regul. Chaotic Dyn.,* 2002, vol. 7, no. 1, pp. 49–60.
15. Le Saux, C., Leine, R. I., and Glocker, Ch., Dynamics of a Rolling Disk in the Presence of Dry Friction, *J. Nonlinear Sci.,* 2005, vol. 15, no. 1, pp. 27–61.
16. Leine, R. I., Experimental and Theoretical Investigation of the Energy Dissipation of a Rolling Disk during Its Final Stage of Motion, *Arch. Appl. Mech.,* 2009, vol. 79, no. 11, pp. 1063–1082.
17. Leine, R. I. and Glocker, Ch., A Set-Valued Force Law for Spatial Coulomb – Contensou Friction, *Eur. J. Mech. A Solids,* 2003, vol. 22, no. 2, pp. 193–216.
18. Leine, R. I. and Nijmeijer, H., *Dynamics and Bifurcations of Non-Smooth Mechanical Systems,* Lect. Notes Appl. Comput. Mech., vol. 18, Berlin: Springer, 2004.
19. Magnus, K., *Kreisel: Theorie und Anwendungen,* Berlin: Springer, 1971.
20. Moffatt, H. K., Euler's Disk and Its Finite-Time Singularity, *Nature,* 2000, vol. 404, no. 6780, pp. 833–834.
21. Moffatt, H. K. and Shimomura, Y., Classical Dynamics: Spinning Eggs — A Paradox Resolved, *Nature,* 2002, vol. 416, no. 6879, pp. 385–386.
22. Moffatt, H. K., Shimomura, Y., and Branicki, M., Dynamics of an Axisymmetric Body Spinning on a Horizontal Surface: 1. Stability and the Gyroscopic Approximation, *Proc. Roy. Soc. London Ser. A,* 2004, vol. 460, no. 2052, pp. 3643–3672.
23. Moreau, J. J., Unilateral Contact and Dry Friction in Finite Freedom Dynamics, in *Non-Smooth Mechanics and Applications,* J. J. Moreau, P. D. Panagiotopoulos (Eds.), CISM Courses and Lectures, vol. 302, Wien: Springer, 1988, pp. 1–82.
24. Nützi, G. E., Non-Smooth Granular Rigid Body Dynamics with Applications to Chute Flows, *PhD Thesis,* Zürich: ETH Zürich, 2016.
25. O'Reilly, O. M., The Dynamics of Rolling Disks and Sliding Disks, *Nonlinear Dyn.,* 1996, vol. 10, no. 3, pp. 287–305.
26. Poinsot, L., *Théorie nouvelle de la rotation des corps,* Paris: Bachelier, 1834.
27. Przybylska, M. and Rauch-Wojciechowski, S., Dynamics of a Rolling and Sliding Disk in a Plane: Asymptotic Solutions, Stability and Numerical Simulations, *Regul. Chaotic Dyn.,* 2016, vol. 21, no. 2, pp. 204–231.
28. Rauch-Wojciechowski, S., What Does It Mean to Explain the Rising of the Tippe Top?, *Regul. Chaotic Dyn.,* 2008, vol. 13, no. 4, pp. 316–331.
29. Rockafellar, R. T., *Convex Analysis,* Princeton, N.J.: Princeton Univ. Press, 1970.
30. Tiaki, M. M., Hosseini, S. A. A., and Zamanian, M., Nonlinear Forced Vibrations Analysis of Overhung Rotors with Unbalanced Disk, *Arch. Appl. Mech.,* 2016, vol. 86, no. 5, pp. 797–817.